Journal of Computational Physics 231 (2012) 1587–1614

Contents lists available at SciVerse ScienceDirect

Journal of Computational Physics

journal homepage: www.elsevier.com/locate/jcp

Adaptive ANOVA decomposition of stochastic incompressible and compressible flows

Xiu Yang [a], Minseok Choi [a], Guang Lin [b], George Em Karniadakis [a,*]

[a] Division of Applied Mathematics, Brown University, Providence, RI 02912, USA
[b] Pacific Northwest National Laboratory, Richland, WA 99352, USA

ARTICLE INFO

Article history:
Received 4 January 2011
Received in revised form 27 September 2011
Accepted 22 October 2011
Available online 11 November 2011

Keywords:
Rayleigh–Benard convection
Supersonic flow
Uncertainty quantification
High dimensions
Sparse grids

ABSTRACT

Realistic representation of stochastic inputs associated with various sources of uncertainty in the simulation of fluid flows leads to high dimensional representations that are computationally prohibitive. We investigate the use of adaptive ANOVA decomposition as an effective dimension–reduction technique in modeling steady incompressible and compressible flows with nominal dimension of random space up to 100. We present three different adaptivity criteria and compare the adaptive ANOVA method against sparse grid, Monte Carlo and quasi-Monte Carlo methods to evaluate its relative efficiency and accuracy. For the incompressible flow problem, the effect of random temperature boundary conditions (modeled as high-dimensional stochastic processes) on the Nusselt number is investigated for different values of correlation length. For the compressible flow, the effects of random geometric perturbations (simulating random roughness) on the scattering of a strong shock wave is investigated both analytically and numerically. A probabilistic collocation method is combined with adaptive ANOVA to obtain both incompressible and compressible flow solutions. We demonstrate that for both cases even draconian truncations of the ANOVA expansion lead to accurate solutions with a speed-up factor of three orders of magnitude compared to Monte Carlo and at least one order of magnitude compared to sparse grids for comparable accuracy.

1. Introduction

Stochastic modeling of fluid mechanics problems allows for a broader and more comprehensive understanding of the flow physics compared to deterministic formulations, and it can potentially lead to new approaches in designing thermo-fluidic equipment that operates robustly under uncertain conditions. While significant progress has been made to date in advancing stochastic CFD, most of the processes simulated so far have been modeled by low-dimensional representations of the inputs and outputs, often limiting our ability in probing the intriguing physics of the flow, e.g., the effect of random disturbances of large amplitude and/or small correlation length on flow stability and on momentum and heat transport. These effects require high-dimensional representations in the parametric or random space that often render such simulations computationally prohibitive. Towards this end, progress can be made if the computational complexity of the stochastic problem is reduced by some orders of magnitude, e.g., by estimating the so-called "effective dimensionality" of the flow system, as was done for financial systems using quasi-Monte Carlo theory [1,2]. In this paper we employ the functional ANOVA (ANalysis-Of-VAriance) method [3,4] and evaluate its effectiveness as a dimension–reduction technique for incompressible and compressible

* Corresponding author.
E-mail addresses: george_karniadakis@brown.edu, gk@cfm.brown.edu (G.E. Karniadakis).

0021-9991/$ - see front matter © 2011 Elsevier Inc. All rights reserved.
doi:10.1016/j.jcp.2011.10.028

flow problems. This is motivated by the idea that for many flow systems, only relatively low order correlations between dimensions will significantly impact the solution.

The ANOVA decomposition was introduced by Fisher in 1921 (see, e.g., [5]) and employed for studying U-statistics by Hoeffding [6]. ANOVA has also previously been used in the context of uncertainty quantification in [7] and was formulated in terms of polynomial chaos for solving high-dimensional stochastic PDEs in [8,9]. In particular, in [8] ANOVA was combined with a multi-element probabilistic collocation method (PCM) to represent each expansion term for greater control of accuracy and efficiency of the discrete representation. ANOVA involves splitting a multi-dimensional function into its contributions from different groups of sub-dimensions. The underlying idea involves the splitting of a one-dimensional function approximation space into the constant subspace and the remainder space. The associated splitting for multi-dimensional cases is formed via a tensor-product construction. In practice, one essentially truncates the ANOVA-type decomposition at a certain dimension v, thereby dealing with a series of low-dimensional ($\leqslant v$) approximation problems in lieu of one high-dimensional problem. This type of truncation can make high-dimensional approximation tractable for functions with high nominal dimension N but only low-order correlations among input variables (i.e., $v \ll N$). However, even with severe truncations, e.g., $v = 2$, the ANOVA decomposition of a high-dimensional function includes many thousands of terms, e.g., for a 1000-dimensional function ($N = 1000$) and $v = 2$ we need to evaluate close to half a million terms, see Example 1 in Section 2. To this end, in the current work we aim to reduce further the associated computational complexity by adaptively evaluating the terms in the ANOVA expansion and keep only the most important ones. This approach can reduce the number of terms in the aforementioned example to about 100 – a reduction of more than three orders of magnitude! Clearly, the accuracy of the representation will also be reduced as a function of the truncation dimension and this is problem dependent, hence we need to consider different flow systems – both viscous and inviscid – in order to evaluate the relationship between economical adaptive ANOVA representations and accuracy in the main statistics, i.e., the mean and variance of the stochastic solution.

We consider two prototype flow problems, which have been well-studied with deterministic CFD. The first is a thermally-driven incompressible viscous flow while the second is shock scattering by a wedge surface. In the former, we include the stochasticity in the thermal boundary conditions whereas in the latter we consider a random geometric boundary representing roughness. So first, we will study stochastic Rayleigh–Benard convection in a finite fluid layer confined between horizontal boundaries. When the geometry is bounded by rigid and perfectly insulating sidewalls then the *critical* Rayleigh number is increased due to stabilizing effects of finite geometry [10–13]. Many previous works on Rayleigh–Benard convection have focused on how the results of classical stability problems concerning steady state flows are affected by small variations of the base state [13]. However, the case where the perturbations are random in space and of finite amplitude has not been addressed; taking the correlation length of the boundary temperature perturbations to be small leads to a high-dimensional problem. Fig. 1 shows contours of the mean temperature in the domain for two different Rayleigh numbers; the lower and upper wall temperatures will be modeled as high-dimensional stochastic processes and the solution will be represented via ANOVA decomposition. In addition, we will compare the adaptive ANOVA method against the sparse grid and Monte Carlo (MC) methods in order to evaluate its relative accuracy and efficiency of each method.

The second prototype problem is inviscid compressible flow, specifically, supersonic flow past a rough wedge. For the smooth wedge, the shock path and pressure distribution can be obtained by simple analytical formulas. However, complex

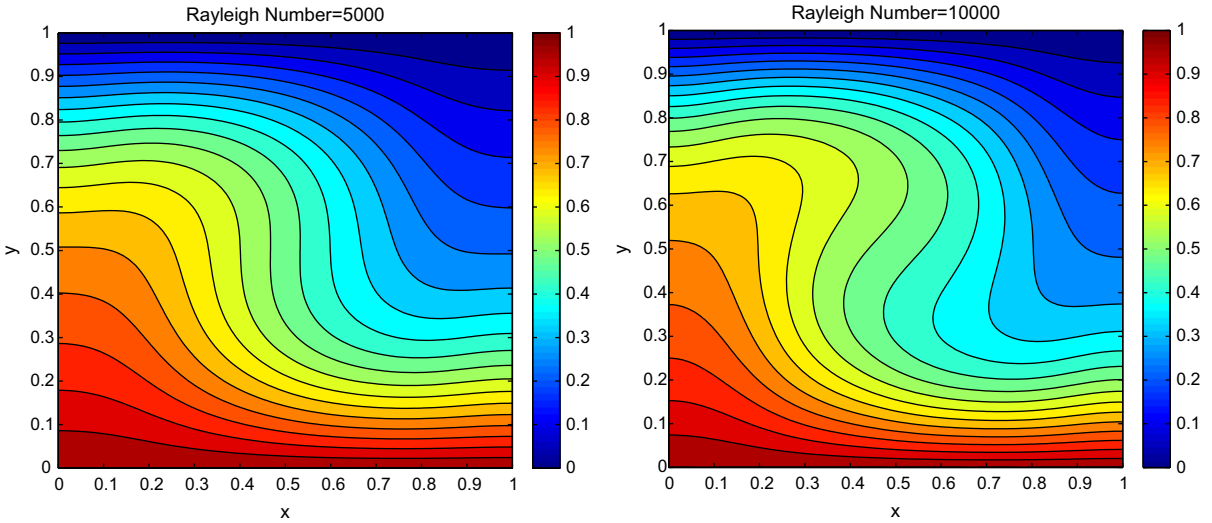

Fig. 1. Contours of the mean temperature for two Rayleigh number $Ra = 5000$ and $Ra = 10{,}000$. The correlation length here is $A = 0.1$ but we also consider the case of $A = 0.01$ while the magnitude of perturbation 0.15 (see Section 3). There exist two possible stable states: counter-clockwise and clockwise motion. Here only the clockwise motion is shown.

shock dynamics is observed when considering a random rough wedge surface. Lighthill [14] and Chu [15] used first-order perturbation analysis to study the case of weak interactions. The first-order theory is adequate only for very small roughness height and does not provide a measure of the *mean* extra force due to roughness, which is assumed to have zero mean, and hence the first-order theory predicts zero mean forces. Lin et al. [16,17] developed a second-order perturbation method to overcome the disadvantages of first-order method and developed semi-analytical formulas to describe the solution for small roughness height. Fig. 2 (from [16]) shows pressure contours of one realization for two different Mach numbers; here we will only focus on the high Mach number case. Similarly to the incompressible flow example, here too we will compare the ANOVA based solution to corresponding solutions obtained by the sparse grid and the quasi-Monte Carlo methods.

This paper is organized as follows: In Section 2 we introduce the standard ANOVA method and propose the adaptive ANOVA method based on three different adaptive criteria. In Section 3 we formulate the stochastic convection problem, present computational results, and compare the adaptive ANOVA method with the sparse grid and MC methods. The effect of correlation length is studied for different cases including a 96-dimensional case. In Section 4 we consider supersonic flow past a rough wedge and compute the extra forces on the wedge. We present both semi-analytical results obtained by the second-order perturbation method as well as numerical results obtained by the WENO method. The effect of correlation length is studied for different cases including a 100-dimensional case. We conclude in Section 5 with a brief summary and discussion. In the appendix we provide some details on the semi-analytical solution of the shock scattering problem.

2. ANOVA decomposition

2.1. Standard ANOVA

The ANOVA method is widely used in statistics. The same idea can be used for interpolation and integration of high dimensional problems as well as stochastic simulations [18,8]. Consider an integrable function $f(\boldsymbol{x})$, $\boldsymbol{x} = (x_1, x_2, \ldots, x_N)$ defined in $I^N = [0,1]^N$, then we have:

Definition. The representation of $f(\boldsymbol{x})$ in a form

$$f(\boldsymbol{x}) = f_0 + \sum_{s=1}^{N} \sum_{j_1 < \cdots < j_s} f_{j_1 \cdots j_s}(x_{j_1}, \ldots, x_{j_s}) \tag{2.1}$$

or equivalently

$$f(\boldsymbol{x}) = f_0 + \sum_{1 \leqslant j_1 \leqslant N} f_{j_1}(x_{j_1}) + \sum_{1 \leqslant j_1 < j_2 \leqslant N} f_{j_1 j_2}(x_{j_1}, x_{j_2}) + \cdots + f_{1,2,\ldots,N}(x_1, x_2, \ldots, x_N) \tag{2.2}$$

is called ANOVA decomposition, if

$$f_0 = \int_{I^N} f(\boldsymbol{x}) \, \mathrm{d}\mu(\boldsymbol{x}), \tag{2.3}$$

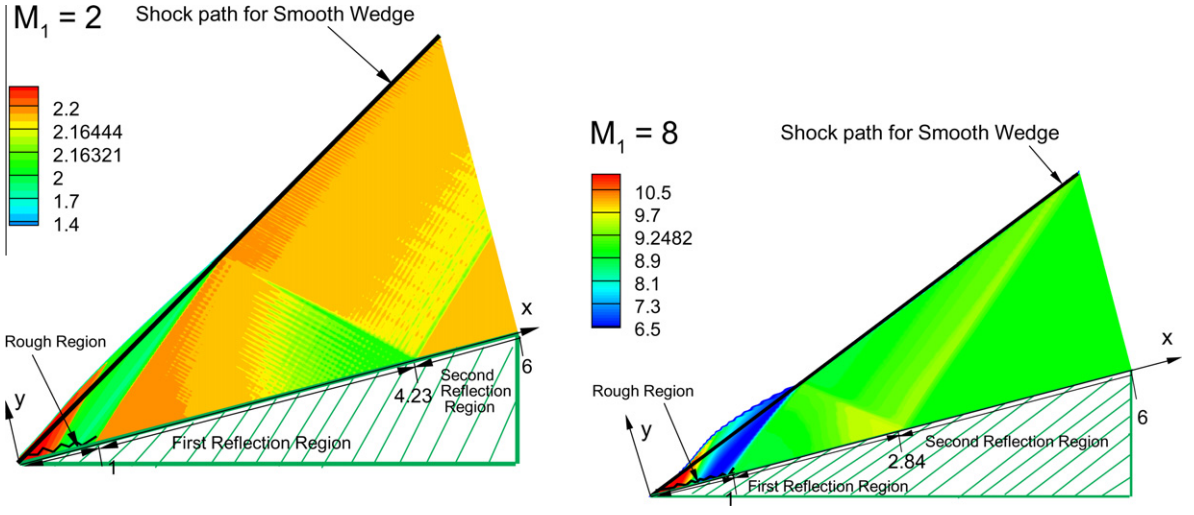

Fig. 2. Pressure contours for $M_1 = 2$ (left) and $M_1 = 8$ (right), where M_1 is the Mach number of the uniform inflow from left. Roughness height $\varepsilon = 0.01$, and correlation length of roughness is $A = 0.1$ but we also consider the case of $A = 0.01$. The pressure contours for $M_1 = 8$ are stretched 4 times perpendicular to the wedge surface for visualization purposes.

and

$$\int_I f_{j_1\cdots j_s}\,\mathrm{d}\mu(x_{j_k}) = 0 \quad \text{for} \quad 1 \leqslant k \leqslant s. \tag{2.4}$$

Here $1 \leqslant j_1 < j_2 < \cdots < j_s \leqslant N$, $j \leqslant s \leqslant N$. We call $f_{j_1}(x_{j_1})$ the first-order term (or first-order component function), $f_{j_1 j_2}(x_{j_1 j_2})$ the second-order term (or second-order component function), etc.

Property 1. *An important property of ANOVA decomposition is the orthogonality of its terms:*

$$\int_{I^N} f_{j_1,\ldots,j_s} f_{k_1,\ldots,k_l}\,\mathrm{d}\mu(\boldsymbol{x}) = 0, \tag{2.5}$$

if $(j_1,\ldots,j_s) \neq (k_1,\ldots,k_l)$. This is a direct consequence of (2.4). The terms in the ANOVA-decomposition are computed as follows:

$$f_S = \int_{I^{N-|S|}} f(\boldsymbol{x})\,\mathrm{d}\mu(\boldsymbol{x}_{S^c}) - \sum_{T\subset S} f_T(\boldsymbol{x}_T), \tag{2.6}$$

where $S = \{j_1, j_2, \ldots, j_s\}$, $|S|$ is the number of elements in S, T is a subset of S and $f_T = f_{j_1 j_2,\ldots,j_t}(x_{j_1}, x_{j_2}, \ldots, x_{j_t})$.

Property 2. *The variance of f is the sum of the variances of all the decomposition terms:*

$$\sigma^2(f) = \sum_{s=1}^{N}\sum_{|S|=s}\sigma^2(f_S), \quad \sigma^2(f_S) = \int_{I^N} f_S^2\,\mathrm{d}\mu(\boldsymbol{x}), \tag{2.7}$$

or equivalently:

$$\sigma^2(f) = \sum_{1\leqslant j_1\leqslant N}\sigma^2(f_{j_1}) + \sum_{1\leqslant j_1<j_2\leqslant N}\sigma^2(f_{j_1 j_2}) + \cdots + \sigma^2(f_{1,2,\ldots,N}).$$

It is very important that (2.7) holds only when the measure used in the integral of computing the variance is the same as that used in the ANOVA decomposition (2.6). It is probable that $\sigma(f)$ is different from the exact value computed by the standard definition of variance, i.e., the integral with Lebesgue measure.

Remark 3. Computing the ANOVA decomposition, i.e., the constant term from (2.3) and high-order terms from (2.6), can be very expensive for high dimensional problems or complicated $f(\boldsymbol{x})$. Therefore, we use the Dirac measure instead of Lebesgue measure in integrations, i.e., $\mathrm{d}\mu(\boldsymbol{x}) = \delta(\boldsymbol{x}-\boldsymbol{c})\,\mathrm{d}\boldsymbol{x}$, $\boldsymbol{c}\in I^N$. The point "$\boldsymbol{c}$" is called "*anchor point*" and this method is called "*anchored-ANOVA*". Hence, for the constant term we have

$$f_0 = f(\boldsymbol{c}). \tag{2.8}$$

Different choices of anchor points can lead to different approximations of ANOVA decomposition to a function; the authors in [19,20] defined different weights depending on the norm for tensor product functions, proved that the anchor point satisfying certain condition minimizes the error estimate of the approximation of ANOVA decomposition, and presented some numerical examples. It was also shown in [21,22] that ANOVA decomposition with $v = 2$ has a good accuracy if the anchor point is chosen as the mean with respect to the probability density function considered. To this end, we choose the zero point as the anchor point in this paper.

Remark 4. When applying the ANOVA method to stochastic simulation, we denote the highest dimension for the component functions we use in (2.2) with v and approximate $f(\boldsymbol{x})$ with

$$f(\boldsymbol{x}) \approx f_0 + \sum_{j_1\leqslant N} f_{j_1}(x_{j_1}) + \sum_{j_1<j_2\leqslant N} f_{j_1 j_2}(x_{j_1}, x_{j_2}) + \cdots + \sum_{j_1<j_2<\cdots<j_v\leqslant N} f_{j_1 j_2,\ldots,j_v}(x_{j_1}, x_{j_2}, \ldots x_{j_v}). \tag{2.9}$$

Here N is called *nominal dimension*, v is called the truncation or effective dimension, and we use μ to denote the number of collocation points, which coincide with the quadrature points for performing the integration in each dimension.

After we obtain the ANOVA decomposition of a function f, we can approximate the integration of each component function with the values of these functions at the quadrature points based on the corresponding weights. We can also use these quadrature points as the collocation (sampling) points in the probabilistic collocation method (PCM).

2.2. Adaptive ANOVA

Although the standard ANOVA can potentially reduce the computational complexity substantially, it still requires a very large number of sampling points to compute all the terms for a high nominal dimension N. For example, for nominal dimension $N = 100$, the number of sampling points for truncation dimension $v = 2$ and number of collocation points per direction

$\mu = 3$ is $1 + 3 \times \binom{100}{1} + 3^2 \times \binom{100}{2} = 44851$. An efficient way of solving this problem is to develop an adaptive ANOVA decomposition. To this end, we replace the nominal dimension by an ***active dimension*** D_i for each subgroup, i.e., we modify (2.9) to be

$$f(\boldsymbol{x}) \approx f_0 + \sum_{j_1 \leqslant D_1} f_{j_1}(x_{j_1}) + \sum_{j_1 < j_2 \leqslant D_2} f_{j_1 j_2}(x_{j_1}, x_{j_2}) + \cdots + \sum_{j_1 < j_2 < \cdots < j_v \leqslant D_v} f_{j_1 j_2, \ldots, j_v}(x_{j_1}, x_{j_2}, \ldots x_{j_v}). \tag{2.10}$$

In the flow problems we consider here we truncate the expansion with $v = 2$ and in most cases we let $D_1 = N$. We then develop adaptivity criteria to determine the active dimension D_2; see also [21,19]. These criteria depend on the low-order statistics, i.e., mean and variance of the first-order terms in the ANOVA decomposition since they are easy to compute. Specifically, if the nominal dimension is N, the number of collocation points needed for a simulation based on the first-order terms is $\mu N + 1$.

Next, we present how to obtain an estimate of mean and variance of first-order terms in the ANOVA decomposition. Consider $f_1(x_1)$ for instance. Let $\boldsymbol{c}_{-1} = (c_2, c_3, \ldots, c_N)$ and $q_1^1, q_1^2, \cdots, q_1^\mu$ be the quadrature points for one-dimensional approximation (the weights for these quadrature points are generated as well, e.g., Gaussian quadrature). Since we use the Dirac measure when computing the component term, according to (2.6) we have the value of f_1 at the quadrature point:

$$f_1(q_1^1) = f(q_1^1, c_2, c_3, c_4, \ldots, c_N) - f_0, \tag{2.11}$$

and we can readily approximate the mean and standard deviation of f_1. By running the deterministic solver at the sampling point $(q_1^1, \boldsymbol{c}_{-1})$ we can obtain $f(q_1^1, c_2, c_3, c_4, \cdots, c_N)$, while the constant term f_0 is obtained by running the deterministic solver at the pre-selected anchor point. Next, we can compute $f_1(q_1^1)$ by (2.11). Since the weight for this sampling point can be computed based on the quadrature point $q_1^1, q_1^2, \ldots, q_1^\mu$, the mean and variance of f_1 can be obtained after we compute $f(q_1^1), f(q_1^2), \ldots, f(q_1^\mu)$. This process can be applied recursively for computing the mean and variance for all the first-order terms.

Similarly we can compute the second-order terms, e.g., consider the term $f_{1,2}$ at quadrature point $\left(q_1^i, q_2^j\right)$ with $i, j = 1, \ldots, \mu$. We can use (2.6) to obtain:

$$f_{1,2}\left(q_1^i, q_2^j\right) = f\left(q_1^i, q_2^j, c_3, c_4, \ldots, c_N\right) - f_1(q_1^i) - f_2\left(q_2^j\right) - f_0, \tag{2.12}$$

where

$$f_1(q_1^i) = f(q_1^i, c_2, c_3, \ldots, c_N) - f_0,$$
$$f_2\left(q_2^j\right) = f\left(c_1, q_2^j, c_3, \ldots, c_N\right) - f_0.$$

Here we use the tensor product rule to obtain the quadrature points for higher dimension terms, therefore the weights for these quadrature points can be obtained easily. Other methods like sparse grids can also be used. In this paper we only use the tensor product rule for high order terms in ANOVA decomposition to demonstrate our method.

We can now summarize the above steps in the following algorithm:

Algorithm 1. Adaptive (anchored) ANOVA

1: Select the anchor point $\boldsymbol{c}$ and run the deterministic solver at this sampling point to obtain the constant term in the ANOVA decomposition (according to Eq. (2.8)) for the quantity of interest f_0.
2: Select μ collocation points q_1^i according to the probability measure and generate corresponding weights w_i, $i = 1, \ldots, \mu$. Run the deterministic solver at the sampling points to obtain the value of f_1 at the quadrature points in the ANOVA decomposition using Eq. (2.11). Repeat the same procedure for $f_2, f_3, \ldots, f_N$.
3: Compute the necessary statistics like mean and standard deviation required in the adaptivity criterion to determine the active dimension D_2 for selecting the important second-order terms.
4: Use the tensor product rule to generate new sampling points (e.g., $\left(q_1^i, q_2^j, c_3, c_4, \ldots, c_N\right)$ in (2.12)) and run the deterministic solver at the sampling points then compute the second-order terms in the ANOVA decomposition using Eq. (2.12).
5: Repeat the above steps, if needed, for further selection of high-order terms based on the computed statistical values from first- and second-order terms.

Now we have obtained the values of function f at all the collocation points and since each point is equipped with a corresponding weight we can estimate the mean, standard deviation and other statistical values of f. For example, the mean of f is approximated by

$$\int_{I^N} f(\boldsymbol{x})\, \mathrm{d}x \approx \sum_i f(\boldsymbol{q}^i) w_i, \tag{2.13}$$

where $f(\boldsymbol{x}_i)$ is obtained by the deterministic solver, $\boldsymbol{q}^i$ are collocation points and w_i are corresponding weights.

Remark 5. In step 2 we compute all the first-order terms because we set the active dimension $D_1 = N$. This can be modified if $D_1 < N$. Also, by setting $v = 2$ we have that the highest order we use is two, but this can be modified if a larger v is required; similar to step 3, we compute the necessary statistical values for the proper criterion to select higher order terms.

Remark 6. In practice, we do not need all the second-order terms in (2.10) so we use fewer terms as shown in step 3, e.g., for the applications in this paper we approximate $f(\boldsymbol{x})$ by:

$$f(\boldsymbol{x}) \approx f_0 + \sum_{j_1 \leqslant D_1} f_{j_1}(x_{j_1}) + \sum_{(j_1 j_2) \in \mathcal{F}} f_{j_1 j_2}(x_{j_1}, x_{j_2}), \tag{2.14}$$

where

$$\mathcal{F} = \{(j_1, j_2) | j_1 < j_2 < D_2, f_{j_1 j_2} \text{ satisfies an adaptivity criterion.}\}$$

Similarly, if $v > 2$ we can continue using proper adaptivity criteria to decide set $\mathcal{G}, \cdots$ such that (2.10) can be simplified as

$$f(\boldsymbol{x}) \approx f_0 + \sum_{j_1 \leqslant D_1} f_{j_1}(x_{j_1}) + \sum_{(j_1 j_2) \in \mathcal{F}} f_{j_1 j_2}(x_{j_1}, x_{j_2}) + \sum_{(j_1 j_2 j_3) \in \mathcal{G}} f_{j_1 j_2 j_3}(x_{j_1}, x_{j_2}, x_{j_3}) + \cdots \tag{2.15}$$

We list three possible adaptive criteria here:

Criterion 1. Let $T_1 = \sum_{j=1}^{N} \sigma^2(f_j)$, which is the sum of the variances of all the first-order terms. The active dimension D_2 should satisfy:

$$\sum_{j=1}^{D_2} \sigma^2(f_j) \geqslant p T_1, \tag{2.16}$$

where p is a proportionality constant with $0 < p < 1$ and is very close to 1. This criterion is similar to the criterion used in [23] where $\sigma^2(f)$ instead of T_1 is used on the right-hand-side of (2.16) and p is set to be 0.99. As an example, Fig. 11 shows the standard deviation for the first-order terms $f_j(x_j)$ in the ANOVA decomposition of the extra lift and drag for the compressible problem we study in the current work. Since we are interested in these two variables we should consider them simultaneously. It is also clear that since we replace $\sigma^2(f)$ with T_1 we should use larger p, because typically the sum of variances of the first-order terms should be less than that of the function itself. According to Remark 6, we need to find a set $\mathcal{F}$, which is accomplished by computing

$$\gamma_{j_1 j_2} = \frac{\sigma^2(f_{j_1 j_2})}{\sum_{j=1}^{D_1} \sigma^2(f_j)}, \tag{2.17}$$

and bounding $\gamma_{j_1 j_2}$ with a predefined error threshold θ_2^1 (superscript i means criterion i).

Criterion 2. Ma and Zabaras [21] use the mean of component function f_S as the indicator to determine the active ANOVA terms. Let

$$\gamma_j = \frac{|\mathbb{E}(f_j)|}{|f_0|}, \tag{2.18}$$

where the pre-defined error threshold θ_1^2 is used to bound γ_j, i.e., $\gamma_j \leqslant \theta_1^2$. If γ_j are monotonically decreasing with respect to j or monotonically decreasing from some j and we set $D_2 \geqslant j$, then (2.18) can be equivalently written as

$$\sum_{i=j}^{D_2} |\mathbb{E}(f_j)| \geqslant p \sum_{j=0}^{N} |\mathbb{E}(f_j)|, \tag{2.19}$$

where p is a proportionality constant with $0 < p < 1$. For instance, the supersonic flow we study in the paper γ_j are positive and monotonically decreasing from some j. Several choices of p and corresponding D_2 are listed in Table 6. Then, for a further selection of the second-order terms, Ma and Zabaras also used

$$\gamma_{j_1 j_2} = \frac{|\mathbb{E}(f_{j_1 j_2})|}{\sum_{j=0}^{D_1} |\mathbb{E}(f_j)|}, \tag{2.20}$$

where $\gamma_{j_1 j_2}$ is bounded by a pre-defined error threshold θ_2^2.

Remark 7. The description for Criterion 2 is different from that in [21] but they are equivalent for the problems we study in this paper. Moreover, another form (similar to (2.18)) of deciding important first-order terms in Criterion 1 is to compute $\gamma_j = \sigma^2(f_j)/T_1$ and bound γ_j with predefined threshold θ_1^1.

Criterion 3. Zhang et al. [19] proposed a criterion for tensor product functions

$$f(\boldsymbol{x}) = \prod_{j=1}^{N} f^{(j)}(x_j), \quad x_j \in [0,1],$$

which is used in the analysis of ANOVA method. Consider

$$\gamma_j = \frac{\sigma^2(f^{(j)})}{\mathrm{E}(f^{(j)})^2}, \quad \text{if} \quad \mathbb{E}(f^{(j)}) \neq 0, \quad 1 \leqslant j \leqslant N. \tag{2.21}$$

A pre-defined threshold θ_1^3 is set and we only use the first-order terms with $\gamma_j > \theta_1^3$. Similar to Criterion 2, if γ_j is monotonically decreasing with respect to j or monotonically decreasing from some j and we set $D_2 \geqslant j$ then (2.21) can equivalently be written as

$$\sum_{j=1}^{D_2} \gamma_j \geqslant p\left(1 + \sum_{j=1}^{N} \gamma_j\right). \tag{2.22}$$

When selecting second-order terms, we set a pre-defined threshold θ_2^3 and use the criterion

$$\frac{\gamma_j \gamma_k}{1 + \sum_{j=1}^{N} \gamma_j + \sum_{j \neq k} \gamma_j \gamma_k} \geqslant \theta_2^3, \tag{2.23}$$

to determine which terms to use. This criterion is very efficient for tensor product functions. We list this criterion here and will compare the performance of Criterions 1 and 2 with it for a tensor product function in Example 1. In real practice we do not use it since we do not have the explicit expression of the solution. Also, even if we have it, the solution need not be a tensor product function.

Remark 8. When we employ the above criteria to applications we replace the mean and variance of component function f_j with their L_2 norm values on the physical domain.

Example 1. We present a simple example for a 1000-dimensional function to illustrate the proposed adaptive criteria using standard ANOVA and anchored ANOVA. Consider the Sobol function [18]

$$f(\boldsymbol{x}) = \prod_{k=1}^{N} f^{(k)}(x_k), \quad x_k \in [0.1], \tag{2.24}$$

where $N = 1000, f^{(k)}(x_k) = \frac{|4x_k - 2| + a_k}{1 + a_k}$ and $a_k = k^2$. Note that the coefficients a_k in this paper are different from those in [18] where $a_k = O(k)$. Three cases with $a_k = O(1)$, $O(k)$ and $O(k^2)$ were considered in [20] and it was explained how different coefficients lead to different convergence rates with respect to the truncation dimension. Then the mean and variance of the function f are readily computed: $\mathbb{E}(f) = 1$ and $\sigma^2(f) = 0.10395$. We test Criterions 1 and 3 using standard ANOVA and Criterions 1 and 2 using anchored ANOVA. For *anchored* ANOVA we use an anchor point $\boldsymbol{c} = (c_1, c_2, \ldots, c_N)$ such that it satisfies $f^{(k)}(c_k) = \frac{\lambda_k^2 + \tau_k^2}{\tau_k}$ where λ_k^2, τ_k is the variance and the mean of $f^{(k)}$, respectively [20]. We compute the error of the variance defined by $|\sigma^2(f) - \sum_S \sigma^2(f_S)|$ and estimate how many terms are selected among all second-order terms. Without adaptivity we need $499,500 = \binom{1000}{2}$ second-order terms. Note that Criterion 2 cannot be used for standard ANOVA since the mean of each ANOVA terms is always zero as in (2.4), hence no terms will be selected. Both Tables 1 and 2 show that just a few second-order terms out of 499,500 terms are needed to achieve at least 10^{-3} accuracy for the variance error. In order to get better accuracy we would need smaller threshold and hence more terms. For standard ANOVA in Table 1 both Criterions 1 and 3 give the same order of magnitude of error with almost the same number of second-order terms selected. This is also true for anchored ANOVA as shown in Table 2. However, the error for anchored ANOVA is larger than the one for standard ANOVA even if it needs more terms since the anchored ANOVA approximation to the function is worse than the standard ANOVA approximation. Tables 1 and 2 also show that $\theta_2^i, (i = 1, 2, 3)$ does not have a significant impact on the variance error for either the standard or the anchored ANOVA.

Table 1
Variance error and size of selected set $\mathcal{F}$ using *standard* ANOVA for the Sobol function. $p = 0.999$. $|\mathcal{F}|$ is the cardinality of $\mathcal{F}$.

Criterion 1	θ_2^1	1e−7	1e−6	1e−5	1e−4
	error	2.0170e−5	2.05217e−5	2.3990e−5	5.2835e−5
	$\lvert\mathcal{F}\rvert$	34	25	16	8
Criterion 3	θ_2^3	1e−7	1e−6	1e−5	1e−4
	error	4.6856e−5	1.2148e−4	2.3682e−4	5.5905e−4
	$\lvert\mathcal{F}\rvert$	15	6	3	1

Table 2
Variance error and size of selected set $\mathcal{F}$ using *anchored* ANOVA for the Sobol function. The anchor point is chosen as described in the text. $p = 0.9999$.

Criterion 1	θ_2^1	1e−7	1e−6	1e−5	1e−4
	error	7.0763e−3	7.0751e−3	7.0648e−3	7.0243e−3
	$\lvert\mathcal{F}\rvert$	76	45	19	8
Criterion 2	θ_2^2	1e−7	1e−6	1e−5	1e−4
	error	7.0747e−3	7.0636e−3	7.0118e−3	6.7630e−3
	$\lvert\mathcal{F}\rvert$	42	18	7	2

Remark 9. We note that the idea of selecting the important dimension is similar to the traditional sensitivity analysis. For example, Sobol's method [18] uses $Var(f_i)/Var(f)$ to measure the sensitivity of factor x_i (or term f_i) while our Criterion 1 replaces the denominator with $\sum_{1\leqslant i\leqslant N} Var(f_i)$. Once the decomposition of f is determined, the selection of the (constant) denominator will not affect the importance of each term (or equivalently, the sensitivity of the corresponding factor). The main difference is that the anchored-ANOVA decomposition based on Dirac measure is different from the traditional ANOVA decomposition based on Lebesgue measure. This difference can lead to different choices of importance dimensions. As has been mentioned in Remark 3, the selection of the anchor point is the key point, and we refer the interested reader to literatures listed in Remark 3.

In the next two sections we apply the adaptive criteria to two prototype problems in fluid mechanics.

3. Incompressible flow: stochastic convection

In this section, we consider a classical problem in fluid mechanics describing incompressible flow driven by thermal gradients. A similar problem was considered in [24,25] in the context of stochastic modeling based on polynomial chaos but using only a small number of dimensions (less than 4) in random space. Here, we demonstrate that we can deal with arbitrarily complex stochastic boundary conditions modeled as stochastic processes with as many as 96 dimensions in random space. This allows us to examine the effect of the correlation length on the momentum and heat transport of this problem.

3.1. Governing equations

Let us consider two-dimensional steady states governed by the Oberbeck–Boussinesq approximation written in terms of the vorticity transport equation in streamfunction-only formulation [26]

$$-\frac{\partial\phi}{\partial y}\frac{\partial(\nabla^2\phi)}{\partial x}+\frac{\partial\phi}{\partial x}\frac{\partial(\nabla^2\phi)}{\partial y}=-Pr\nabla^4\phi+RaPr\frac{\partial T}{\partial x}, \tag{3.1}$$

$$\frac{\partial\phi}{\partial y}\frac{\partial T}{\partial x}-\frac{\partial\phi}{\partial x}\frac{\partial T}{\partial y}=\nabla^2 T, \tag{3.2}$$

where $\phi(x,y,t)$ denotes the dimensionless streamfunction, $T(x,y,t)$ denotes the dimensionless temperature field, and Ra and Pr are the Rayleigh and the Prandtl numbers, respectively.

In Fig. 3 we show a sketch of the geometry and the boundary conditions associated with the system (3.1). The quantity g denotes the acceleration of gravity, which acts vertically downwards, in the direction of decreasing y. The sidewalls of the cavity are assumed to be adiabatic while the horizontal walls are subject to random temperature distributions. The velocity boundary conditions are assumed to be of no-slip type, i.e., $\partial\phi/\partial x = \partial\ \phi/\partial y = 0$ at solid walls. It is convenient to transform the non-homogeneous temperature boundary conditions at the horizontal walls into homogeneous ones. This is easily achieved by defining

$$T^*(x,y;\omega)\overset{\text{def}}{=}T(x,y;\omega)+(y-1)(g_1(x;\omega)+1)-yg_2(x;\omega), \tag{3.3}$$

where $g_1(x;\omega)$ and $g_2(x;\omega)$ are assumed to be finite-dimensional random processes satisfying adiabatic boundary conditions at $x = 0$ and $x = 1$, i.e.,

$$\left.\frac{\partial g_i}{\partial x}\right|_{x=0,1}=0,\quad \text{for}\quad i=1,2. \tag{3.4}$$

Eq. (3.3) can be inverted to give

$$T=T^*+(1-y)(g_1+1)+yg_2 \tag{3.5}$$

from which we obtain

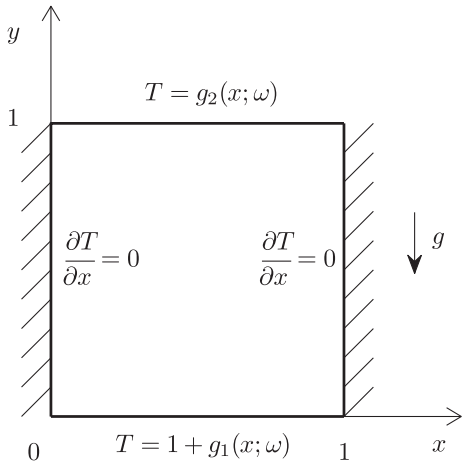

Fig. 3. Schematic of the geometry and dimensionless temperature boundary conditions. The random perturbations g_1 and g_2 are assumed to have zero mean Gaussian processes. The velocity boundary conditions are of no-slip type, i.e., $\phi = \partial\phi/\partial x = \partial\phi/\partial y = 0$ at the solid walls.

$$\frac{\partial T}{\partial x} = \frac{\partial T^*}{\partial x} + y\left(\frac{\partial g_2}{\partial x} - \frac{\partial g_1}{\partial x}\right) + \frac{\partial g_1}{\partial x}, \tag{3.6}$$

$$\frac{\partial T}{\partial y} = \frac{\partial T^*}{\partial y} + (g_2 - g_1) - 1, \tag{3.7}$$

$$\nabla^2 T = \nabla^2 T^* + y\left(\frac{\partial^2 g_2}{\partial x^2} - \frac{\partial^2 g_1}{\partial x^2}\right) + \frac{\partial^2 g_1}{\partial x^2}. \tag{3.8}$$

A substitution of Eqs. (3.6)–(3.8) into Eqs. (3.1) and (3.2) yields the system

$$-\frac{\partial\phi}{\partial y}\frac{\partial(\nabla^2\phi)}{\partial x} + \frac{\partial\phi}{\partial x}\frac{\partial(\nabla^2\phi)}{\partial y} = RaPr\left(\frac{\partial T^*}{\partial x} + y\left(\frac{\partial g_2}{\partial x} - \frac{\partial g_1}{\partial x}\right) + \frac{\partial g_1}{\partial x}\right) - Pr\nabla^4\phi, \tag{3.9}$$

$$\frac{\partial\phi}{\partial y}\left(\frac{\partial T^*}{\partial x} + y\left(\frac{\partial g_2}{\partial x} - \frac{\partial g_1}{\partial x}\right) + \frac{\partial g_1}{\partial x}\right) - \frac{\partial\phi}{\partial x}\left(\frac{\partial T^*}{\partial y} + (g_2 - g_1) - 1\right) = \nabla^2 T^* + y\left(\frac{\partial^2 g_2}{\partial x^2} - \frac{\partial^2 g_1}{\partial x^2}\right) + \frac{\partial^2 g_1}{\partial x^2}, \tag{3.10}$$

with homogeneous boundary conditions. These equations admit an integral representation, where ϕ and T^* are expressed as a linear combination of normalized eigenfunctions, which automatically satisfy all the boundary conditions as well as the continuity equation. A system of ordinary differential equations are derived through the Galerkin projection onto normalized eigenfunctions; see [13,27,28] for more details.

A main quantity of interest is the local heat transfer between the horizontal wall and the fluid. This is quantified in terms of random local Nusselt number defined as

$$Nu_x = -\frac{\partial T}{\partial y}. \tag{3.11}$$

Then, the integrated Nusselt number is represented by

$$Nu = \int_0^1 Nu_x \, dx. \tag{3.12}$$

In order to represent the stochastic boundary condition at the horizontal walls the Karhunen–Loeve (KL) decomposition is used. The finite second-order random process $h(x,\omega)$ representing g_1 and g_2 for the convection problem admits the KL decomposition:

$$h(x,\omega) = \bar{h}(x) + \sum_{i=1}^{\infty} \sqrt{\lambda_i}\psi_i(x)\xi_i(\omega), \tag{3.13}$$

where $\bar{h}(x)$ is the mean, $\{\xi_i(\omega)\}$ is a set of uncorrelated random variables with mean zero and unit variance, and $\{(\lambda_i, \psi_i(x))\}$ is the eigenpair of the covariance kernel $R_{hh}(x_1,x_2)$:

$$\int R_{hh}(x_1,x_2)\psi_i(x_2)\,dx_2 = \lambda_i\psi_i(x_1). \tag{3.14}$$

For both temperature perturbations at the horizontal walls we use the following Gaussian correlation function (see [26])

$$R_{hh}(x_1, x_2) = \exp\left(-6\frac{(x_1 - x_2)^2}{A^2}\right), \tag{3.15}$$

where A is the correlation length.

We assume that the temperature perturbation g_1 and g_2 as shown in Fig. 3 are random processes with zero mean satisfying adiabatic boundary conditions at $x = 0$ and $x = 1$. The adiabatic condition at the boundary are imposed through the spectral transformation method [29,30]. The correlation length A of the random boundary conditions determines the dimension of random space. Table 3 shows how many dimensions we need to capture 95% of the energy of the random field associated with the eigenvalues of the covariance kernel. Since both the top and lower wall have random boundary temperature with the same correlation length, we need twice as many dimensions as the one in the table for the specified correlation length. Table 3 shows that the smaller the correlation length is the higher is the dimension in random space.

3.2. Computational results

We solve the stochastic convection problem using three different methods: (i) Monte Carlo (MC), (ii) sparse grids, and (iii) ANOVA. The main quantities of interest are the velocity and temperature fields and the Nusselt number on the heated (lower) wall. We use the following parameters: $Ra = 5000$, $\sigma = 0.15$, and $A = 0.01$. According to Table 3 the nominal dimension for $A = 0.01$ would be 96 since there are two random fields on the lower and upper wall. Different correlation lengths have an impact on the system, e.g. Nusselt number on the lower wall as shown in Fig. 4(left). The mean of Nusselt number does not change significantly for these parameters as it is correlated strongly with the Rayleigh number [13], which we keep constant here. However, the variance of the Nusselt number for correlation length $A = 1$ is significantly different from the variances for $A = 0.1$ and $A = 0.01$. Figs. 5 and 6 show the mean and the variance, respectively for the velocity and temperature fields in the domain using three different methods as mentioned above. Note that the steady state of the system is in a clockwise one-roll motion state. It is known that the system has two stable states for Rayleigh number 5000: (i) clockwise and (ii) counter-clockwise one-roll motion [13]. The results shown here consider only a clockwise one-roll motion. We see that the ANOVA method works very well even with a very small number of points compared to a much larger number of sampling points associated with MC, which suggests that the ANOVA method, in particular, can be effective in solving high dimensional incompressible flow problems. Fig. 7 shows that MC method with small number of sampling points does not agree well with other methods with about the same number of collocation points.

Table 3
Correlation length and corresponding number of dimensions of random space required to capture 95% of the energy in random space for a single wall.

A	1	0.1	0.01
Dimension	3	22	48

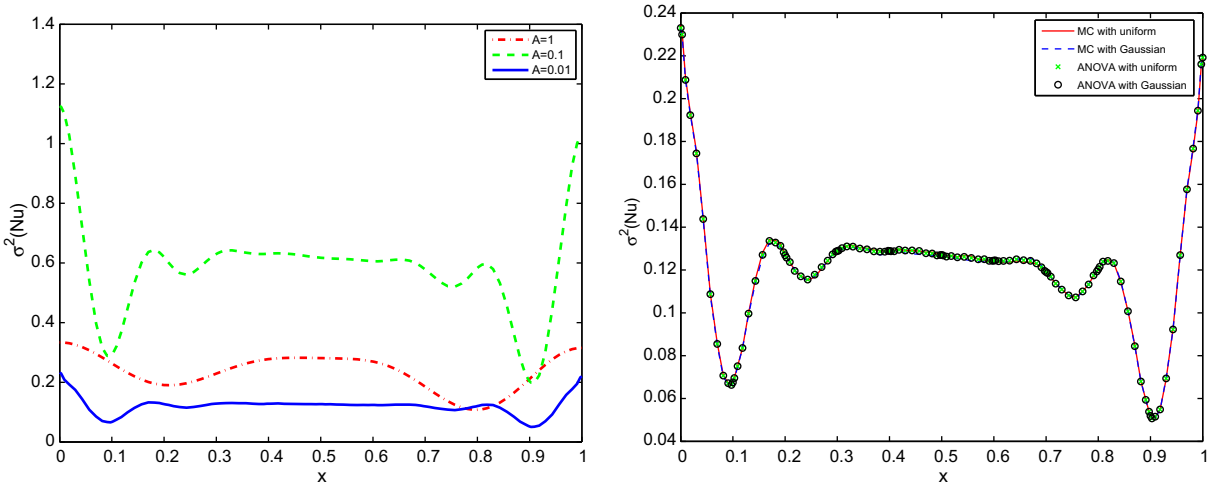

Fig. 4. Left: variance of Nusselt number on the lower wall with respect to three different correlation lengths. Right: variance of Nusselt number on the lower wall with uniform and standard Gaussian random variable for $A = 0.01$. Other parameters are $Ra = 5000$, $\sigma = 0.15$. The right figure shows that the choice of $\xi_i(\omega)$ in (3.13) does not make a difference to the variance of Nusselt number as they appear the same.

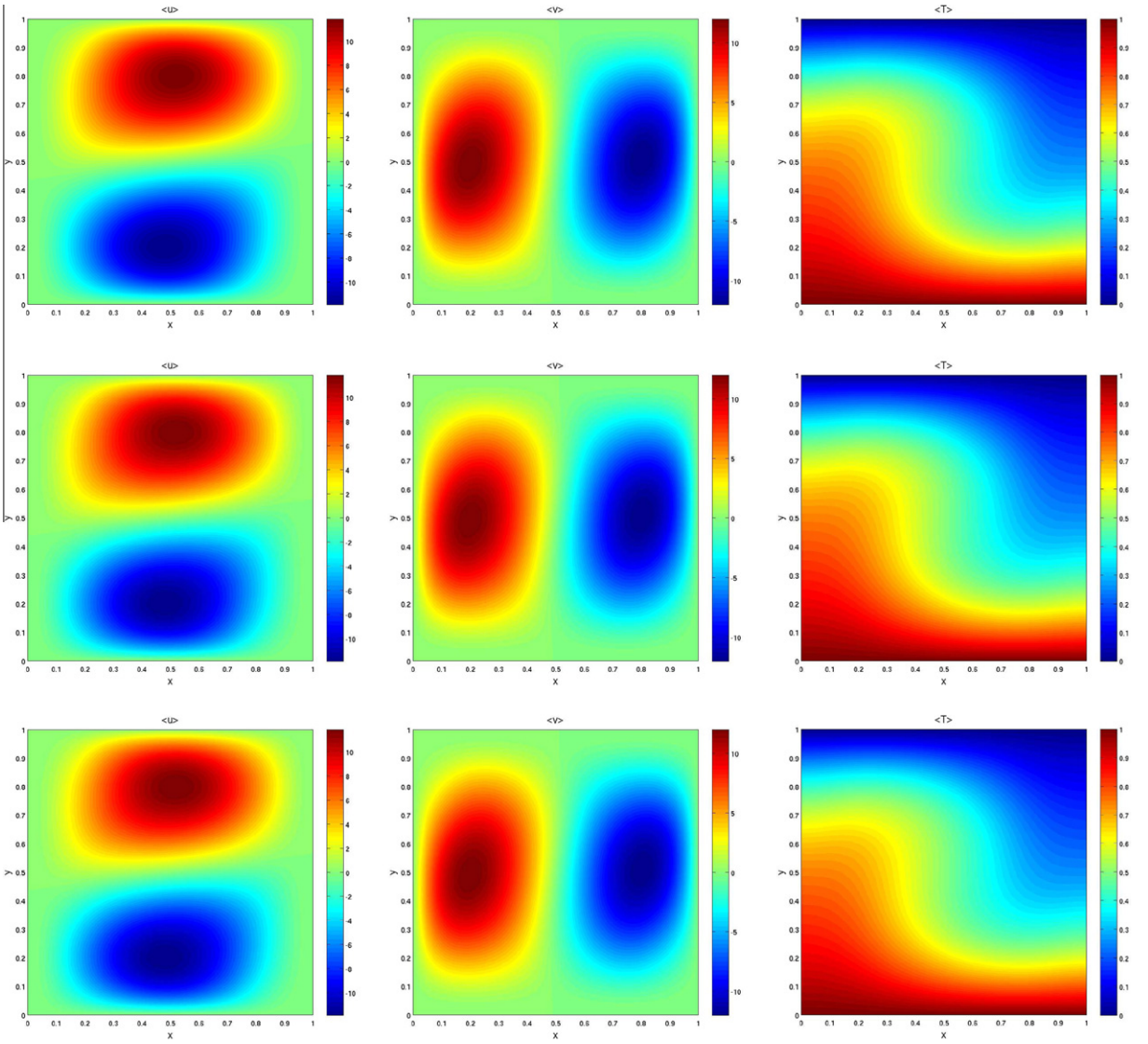

Fig. 5. $Ra = 5000$, $A = 0.01$, $\sigma = 0.15$. $N = 96$ is needed to capture 95% of the energy of the random processes that model the boundary temperatures on the lower and upper walls. The first column represents $\langle u \rangle$; the second column $\langle v \rangle$; the third column $\langle T \rangle$. The first row represents MC method with 90,000 samples, the second row sparse grid method with level 2, and the third row ANOVA method with $\mu = 2$, $v = 1$. The number of grid points used for sparse and ANOVA method is 18,625 and 193, respectively.

Note that in the KL representation (3.13) $\xi_i(\omega)$ is a random variable with mean zero and unit variance. Specifically we treat ξ_i as a *uniform* random variable with mean zero and unit variance, i.e., $\xi_i \approx U[-\sqrt{3}, \sqrt{3}]$. We also tested ξ_i as a *standard Gaussian* random variable and we found that the difference between the two different cases is negligible. In Fig. 4 (right) we plot the variance of Nusselt number on the lower wall with uniform and standard Gaussian random variable for $A = 0.01$.

Here, we summarize the computational details in each step of Algorithm 1:

(1) We first select the anchor point $\boldsymbol{c} = 0$ and solve the system (3.9) and (3.10) at the anchor point in the parametric space defined here by $N = 96$ dimension for $A = 0.01$.
(2) Next, we consider the first-order terms and generate the collocation points and weights $(q_1^i, w_i), i = 1, \ldots, \mu$ based on the Gauss-Legendre quadrature for uniform random variables or Gauss-Hermite for Gaussian random variables (Fig. 4 (right)). Again given a collocation point, we can solve the corresponding deterministic system.
(3) Then, we compute the statistical values of mean and standard deviation required in the adaptivity criterion based on the value of first-order terms f_i at the quadrature points and corresponding weights to determine the active dimension D_2 for selecting the important second-order terms.
(4) Finally proceeding in a similar fashion, we can compute the second-order terms and, if needed, higher-order terms.

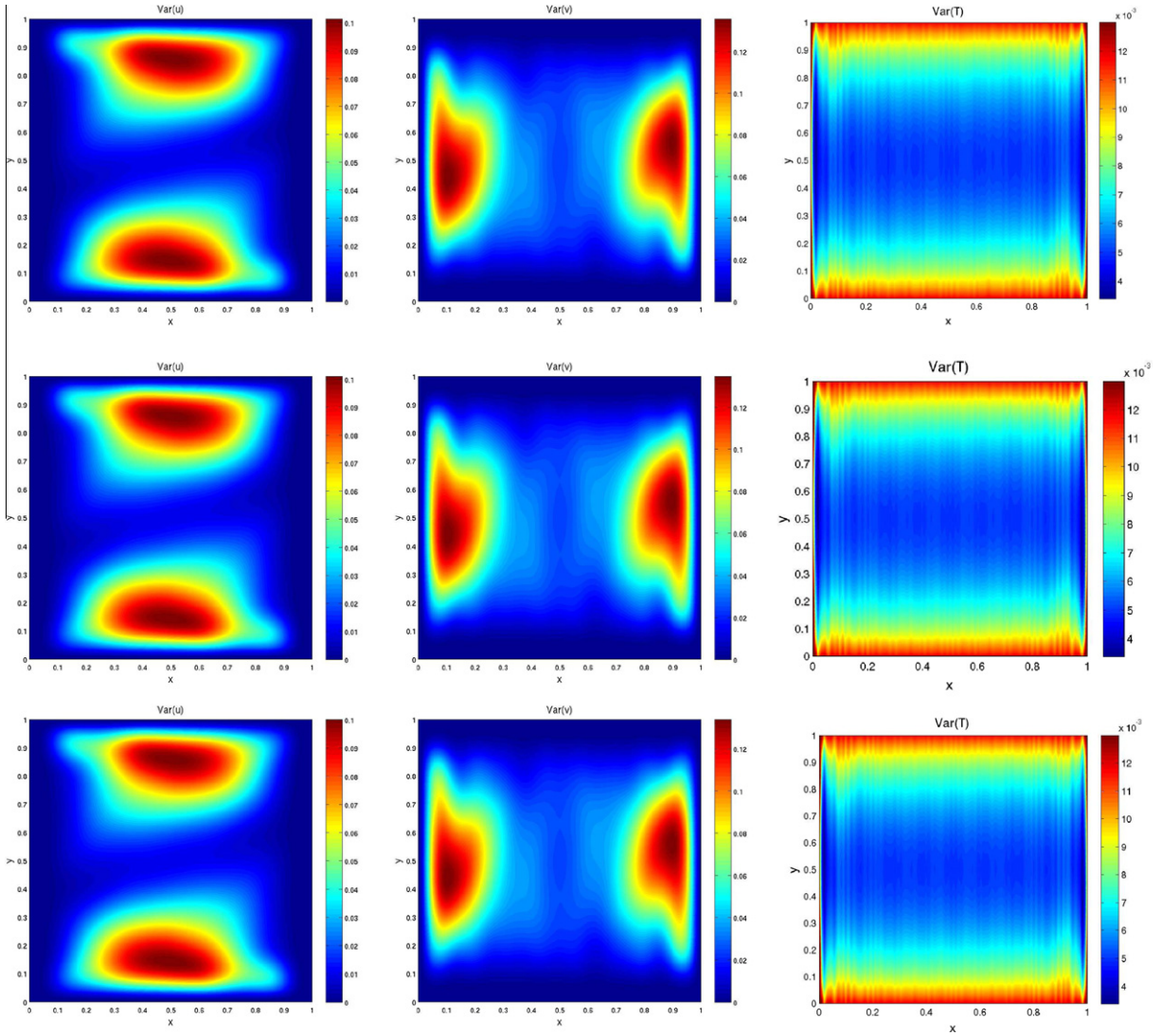

Fig. 6. Same parameters as in previous figure. The first column represents $Var(u)$; the second column $Var(v)$; the third column $Var(T)$. The first row represents MC method with 90,000 samples, the second row sparse grid method with level 2 and single element, and the third row ANOVA method with $\mu = 2$, $v = 1$. The number of grid points used for sparse and anova method is 18,625 and 193, respectively.

Now we present the adaptive ANOVA method and apply Criterion 1 to compute the Nusselt number on the lower wall. We consider the following parameters: $Ra = 5000$, $\sigma = 0.15$, and $A = 0.1$ requiring that the dimension of the random space is 44, and we obtain a stochastic solution by combining the probabilistic collocation method (PCM) with standard ANOVA for polynomial order $\mu = 2$, and truncation dimension $v = 2$. We are interested to evaluate how many terms we can eliminate from the above ANOVA truncation using adaptivity without changing the value of the mean and variance of the Nusselt number significantly. To this end, first we consider only first-order terms, i.e., we totally ignore second-order interactions (and higher), and examine the relative mean and relative variance of first-order ANOVA terms $f_k(x)$, $k = 1,\ldots,N$

$$\gamma_k^1 = \frac{\sigma^2(f_k)}{\sum_{k=1}^N \sigma^2(f_k)}, \quad \gamma_k^2 = \frac{|\mathbb{E}(f_k)|}{\sum_{k=1}^N |\mathbb{E}(f_k)|}.$$

We select the active dimension D_1 such that

$$\gamma_k^1 > \eta, \quad \gamma_k^2 > \eta \tag{3.16}$$

for different values of η. Note that this criterion, in essence, combines Criterions 1 and 2 described in the previous section. Table 4 shows how many dimensions are selected by varying the threshold η. We compute the variance from the selected first-order ANOVA terms according to Eq. (3.16) and compare it with the variance of the Nusselt number for a reference solu-

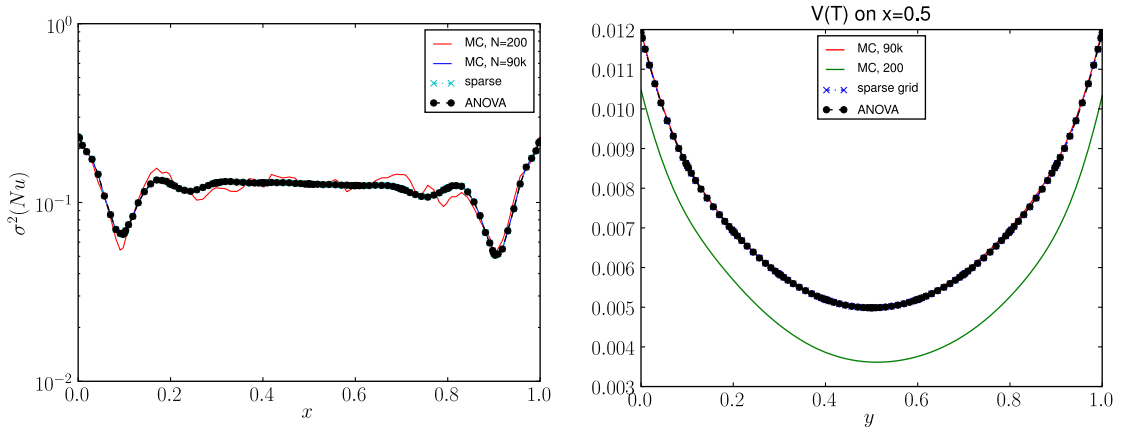

Fig. 7. $Ra = 5000$, $\sigma = 0.15$, $A = 0.01$. Left: variance of Nusselt number on the lower wall. Right: variance of temperature on $x = 0.5$. While MC with 90,000 points (blue solid line) agrees well with ANOVA with $\mu = 2$ and $\nu = 1$ (dotted black circle) and sparse grid with level 1 (about 200 points), MC with 200 points are different from those. The ANOVA and sparse grids give similar results. (For interpretation of the references to colour in this figure legend, the reader is referred to the web version of this article.)

Table 4
Active dimension D_1 satisfying Eq. (3.16).

η	0.1	0.05	0.01
D_1	6	10	20

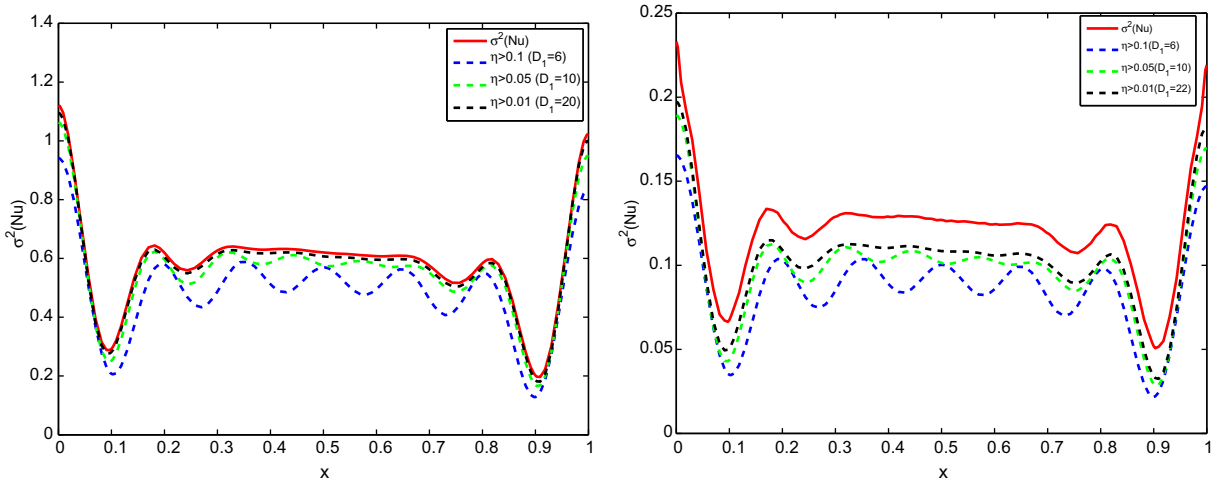

Fig. 8. Variance of Nusselt number using selected first-order ANOVA terms according to (3.16). The more D_1 is (or the smaller η is) the closer the computed variance is to the reference variance (red solid line) derived from Monte Carlo simulation with 90,000 samples. (Left: $\nu = 1$, $A = 0.1$, $\sigma = 0.15$, $N = 44$. Right: $\nu = 1$, $A = 0.01$, $\sigma = 0.15$, $N = 96$. (For interpretation of the references to colour in this figure legend, the reader is referred to the web version of this article.)

tion as shown in Fig. 8. (The reference solution is obtained here using 90,000 MC samples that is within 95% confidence interval.) We see that the lower the threshold η is the closer the variance of the selected first-order ANOVA terms is to the reference variance.

Next, we examine the importance of second-order interactions and their contribution to the Nusselt number. Since the computational cost for first-order terms is small compared to one for second-order terms we can use all first-order terms, i.e., $D_1 = N$ and use Criterion 1 to reduce the number of second-order terms. To this end, we set $D_1 = N, p = 0.99, \theta_2^1 = 10^{-5}$ for $A = 0.1$ and $\theta_2^1 = 10^{-6}$ for $A = 0.01$. We note that while the variance based on the first-order terms f_j for the compressible flow problem (see next section) is monotonically decreasing with respect to the dimension index j, the variance for the convection problem has a non-monotonic behavior. However, the idea of choosing the important terms and determine the active dimension D_2 or $\mathcal{F}$ remains the same.

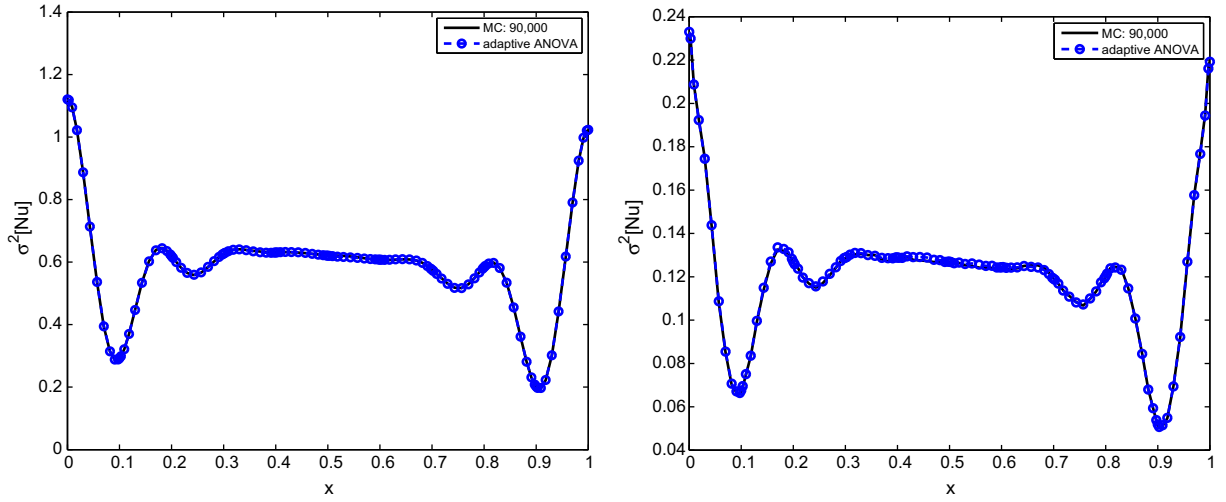

Fig. 9. Left: $A = 0.1$, $N = 44$, $\theta_2 = 10^{-5}$. Right: $A = 0.01$, $N = 96$, $\theta_2 = 10^{-6}$. $\mu = 2$, $v = 2$, $p = 0.99$. We obtain $D_2 = 25$ and $D_2 = 86$, respectively with Criterion 1, and the number of second-order ANOVA terms is 3 and 4, respectively while the number of second-order ANOVA terms without adaptivity is 946 and 4560, respectively. The solid line represents the variance of Nusselt number using MC while the circles correspond to the adaptive ANOVA method based on Criterion 1.

Specifically, for the thresholds used here we obtain $D_2 = 25$ and $|\mathcal{F}| = 3$ for $A = 0.1$ and $D_2 = 86$ and $|\mathcal{F}| = 4$ for $A = 0.01$. Therefore, for $A = 0.1$ the number of points needed for the adaptive ANOVA is 101 while for the standard ANOVA is 3873. These numbers are obtained as follows: For the adaptive ANOVA we have $44 \times 2 + 1$ are the first-order terms plus a constant (here $\mu = 2$ and $D_1 = N = 44$) while the second-order terms are 3×2^2, and the sum of both gives 101 terms. Similarly, for the standard ANOVA we have the same number of first-order terms but the second-order terms are combinations of 44 with 2. Fig. 9 shows the variance of the Nusselt number on the lower wall obtained by MC (90,000 sampling points) and adaptive ANOVA; good agreement is shown. In fact, as shown in Figs. 5 and 6, the ANOVA method even with truncation dimension $v = 1$ is sufficient to obtain a very accurate value of the Nusselt number, and hence the adaptive ANOVA method with $v = 2$ results in a very small set $\mathcal{F}$. Specifically, the L_2 error between the reference solution and the adaptive ANOVA with the above choice is 2.432×10^{-4} while the L_2 error between the reference solution and ANOVA consisted of only first-order terms is 2.887×10^{-4}. Hence, the addition of second-order terms for this case is not important despite the relatively large value of the variance of Nusselt number. As we will see in the next section, this is in contrast to the compressible flow problem where the second-order terms contribute significantly to the variance of the computed forces.

4. Compressible flow: scattering of shock waves

In this section we consider inviscid flow dynamics and focus on the scattering of a strong shock wave due to random roughness on the surface of a half-wedge (see Figs. 2 and 9). Of physical interest here is the effect of roughness on the induced forces on the wedge surface while of numerical interest is the exact form of adaptive ANOVA representation required for different levels of accuracy. The scattering of shock wave is quite different from that of the classical oblique shock problem due to the presence of random roughness.

4.1. Mathematical modeling of random roughness

The roughness length is denoted by d, and we normalize all lengths by d. The roughness starts from the apex of the wedge and the end part of the wedge is smooth. We denote the half wedge angle by θ_0, the unperturbed shock angle for smooth wedge by χ_0, the shock angle for rough wedge at location x by $\chi(x;\omega)$ and the angle between v_s and u_s by $\theta(x;\omega)$ satisfying $\tan\theta = \frac{v_s}{u_s}$, where v_s and u_s are the velocity right after the shock perpendicular and parallel to the wedge, respectively. For a smooth wedge, χ and θ degenerate to χ_0 and θ_0. We denote the incoming flow velocity by W_1 with its normal component $u_1 = W_1 \sin\chi$ and we also denote the velocity there by W_2 and its normal component to the shock by $u_2 = W_2 \sin(\chi - \theta) = W_1 \cos\chi \tan(\chi - \theta)$. Here, u_1, u_2 are the normal components of the velocities going into and coming out of the shock. Fig. 10 shows a sketch of a typical perturbed shock path induced by the randomly rough boundary.

The random roughness is modeled based on a non-dimensional random process $h_m(x;\omega)$ expressed by the KL decomposition:

$$h_m(x;\omega) = \bar{h}_m(x) + \sum_{i=1}^{\infty} \sqrt{\lambda_i}\psi_i(x)\xi_i(\omega), \tag{4.1}$$

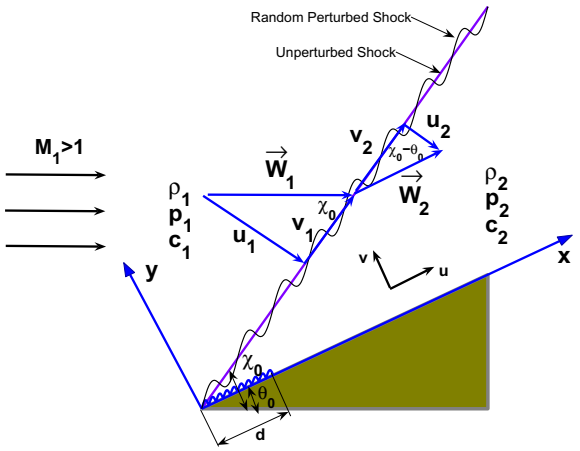

Fig. 10. Sketch of supersonic flow past a wedge with rough surface: definition of coordinate system and notation; shown is also a perturbed shock path and the location of the unperturbed shock corresponding to a smooth wedge surface.

where $\bar{h}_m(x)$ is the mean, $\{\xi_i(\omega)\}$ is a set of uncorrelated random variables with zero mean and unit variance, and ψ_i and λ_i are the eigenvectors and corresponding eigenvalues of the covariance kernel $R_{hh}(x_1,x_2)$:

$$\int R_{hh}(x_1,x_2)\psi_i(x_2)\,\mathrm{d}x_2 = \lambda_i\psi_i(x_1). \tag{4.2}$$

We assume that $\bar{h}_m(x) = 0$, and the roughness height is

$$y(x;\omega) = \varepsilon h(x;\omega) = \varepsilon\frac{h_m}{\max_x(\sigma(h_m))}. \tag{4.3}$$

The covariance kernel $R_{hh}(h_m(x_1;\omega), h_m(x_2;\omega))$ is obtained based on the solution of [17]

$$\frac{\mathrm{d}^4 h_m}{\mathrm{d}x^4} + k^4 h_m = f(x),$$

where x is normalized by the roughness length d, $k = d/A$, A is the correlation length, and the random forcing term $f(x)$ is white noise, i.e., $\mathbb{E}\{f(x_1)f(x_2)\} = \delta(x_1 - x_2)$. Without losing generality, we set $d = 1$. The roughness starts from the apex of wedge and the required boundary conditions for this case are: $h_m(0;\omega) = h'_m(0;\omega) = h_m(1;\omega) = h'_m(1;\omega) = 0$. The eigenvectors are obtained as the solution of the homogeneous equation

$$\frac{\mathrm{d}^4\psi}{\mathrm{d}x^4} - \Lambda^4\psi = 0$$

with boundary condition $\psi(0) = \psi(1) = \psi'(0) = \psi'(1) = 0$ and Λ is the eigenvalue of operator $\mathrm{d}^4/\mathrm{d}x^4$. Such boundary conditions are chosen due to the assumption for second-order perturbation analysis, which states the random roughness and other perturbed quantities are small *and* smooth in the computational domain. The stochastic process $h_m(x;\omega)$ can then be represented by the KL expansion:

$$h_m(x;\omega) = \sum_{n=1}^{\infty}\frac{1}{\Lambda_n^4 + k^4}\psi_n(x)\xi_n(\omega), \tag{4.4}$$

where

$$\psi_n(x) = \cos\Lambda_n x - \cosh\Lambda_n x - \frac{\cos\Lambda_n - \cosh\Lambda_n}{\sin\Lambda_n - \sinh\Lambda_n}(\sin\Lambda_n x - \sinh\Lambda_n x).$$

Here, Λ_n is obtained by solving $\cos\Lambda_n \cosh\Lambda_n = 1$, where $\{\xi_n(\omega)\}$ is a set of uncorrelated random variables with zero mean and unit variance. In practice, the KL expansion is truncated according to the following criterion:

$$\sum_{n=1}^{N}\frac{\Lambda_n}{\Lambda_n^4 + k^4} \geqslant \alpha\sum_{n=1}^{\infty}\frac{\Lambda_n}{\Lambda_n^4 + k^4}, \tag{4.5}$$

where $\alpha = 0.9; 0.95; 0.99$. The number of dimensions for different values of the correlation length and for different values of α are listed in Table 5.

Table 5
Number of dimensions for different values of correlation length at various truncation levels.

α (%)	$A = 1$	$A = 0.1$	$A = 0.01$	$A = 0.001$
90	2	7	79	798
95	3	10	112	1133
99	10	25	253	2537

4.2. Computational results

We consider here the case of Mach number 8 and we follow the set up in [17]; for $A = 0.1$, the nominal dimension $N = 12$ (capturing more than 95% of energy in (4.5)), $\varepsilon = 0.003$, $\theta_0 = 14.7436^\circ$, $\chi_0 = 20.5755^\circ$, and ξ_n used in KL expansion are *uniformly* distributed on $[-\sqrt{3}, \sqrt{3}]$. The contours of pressure for one realization are shown in Fig. 2. We set $\mu = 3$ in the ANOVA decomposition and let the anchor point $\boldsymbol{c} = 0$. This is because from the results in [16,17] we can see that the means for extra lift and drag are very close to 0 and according to the theory in [19], the mean is a good choice (maybe optimal) for anchor point; other choices of anchor points are discussed in [19].

The standard deviation based on the first-order terms f_j for the extra lift and drag are shown in Fig. 11. We use these values in step 3 of the algorithm to determine the necessary second-order terms based on Criterion 1. Similarly, for Criterion 2, we can compute the mean of the first-order terms to be used in step 3; the pattern of the means (not shown in this paper) is similar to the pattern of standard deviations. Both the means and standard deviations are monotonically decreasing when $j \geqslant 2$, hence we can use (2.16) and (2.19) to adaptively select terms.

Several choices of threshold p and corresponding D_2 for Criterions 1 and 2 are listed in Table 6. We set $D_2 = 6$ in order to compare with the sparse grid method and demonstrate the convergence of the adaptive method. Our tests show that $\theta_2^1 = 5.0 \times 10^{-5}$ (i.e., 0.005%) is a good threshold for Criterion 1 and $\theta_2^2 = 1.0 \times 10^{-3}$ (i.e., 0.1%) is a good threshold for Criterion 2. With these thresholds, the estimates of mean and standard deviation of the extra lift and drag are more accurate than for other values. Both criteria lead to the same selection of second-order terms, and hence a good approximation of $f(\boldsymbol{x})$ turns out to be

$$f(\boldsymbol{x}) \approx f_0 + \sum_{j=1}^{12} f_j(x_j) + \sum_{j=2}^{5} f_{1,j}(x_1, x_j) + \sum_{j=3}^{6} f_{2,j}(x_2, x_j) + \sum_{j=4}^{5} f_{3,j}(x_3, x_j), \tag{4.6}$$

where $\boldsymbol{x}$ refers to the random point, and $f(\boldsymbol{x})$ denotes either the extra lift $\Delta L(\boldsymbol{x})$ or extra drag $\Delta D(\boldsymbol{x})$. The number of collocation points used in the different simulations are shown in Tables 7 and 8 for the sparse grid method and adaptive ANOVA method, respectively. We can see that even though the nominal dimension is not large, the number of collocation points required by the sparse grid method increases very quickly as the level increases. For the adaptive ANOVA method, since the active dimension D_2 and the number of collocation points μ are small, the increase of the collocation points is much slower. For comparison, we note that if we use the standard ANOVA method with $\mu = 3$, $\nu = 2$, i.e., we use all the second-order terms, the number of points is 631.

Here, we summarize the computational details in each step of Algorithm 1:

(1) We first select the anchor point $\boldsymbol{c} = 0$ and run the deterministic solver at this anchor point to obtain the constant term f_0 in the ANOVA decomposition (according to Eq. (2.8)). In this case f is the extra pressure Δp.

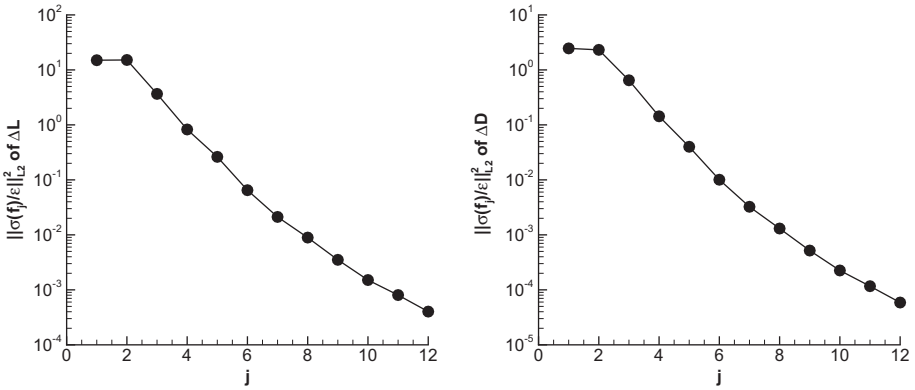

Fig. 11. Standard deviation of extra lift (left) and drag (right) for first-order terms f_j of ANOVA decomposition. $A = 0.1$, $N = 12$, $\mu = 3$. Only the first-order terms are needed when selecting the second-order terms. This is the third step in Algorithm 1.

Table 6
Threshold p and corresponding active dimension D_2 for different criteria.

Criterion 1	p	0.997	0.998	0.999
	D_2	5	6	7
Criterion 2	p	0.97	0.98	0.99
	D_2	5	6	7

Table 7
Number of collocation points for Smolyak sparse grid method: $A/d = 0.1$ and nominal dimension $N = 12$.

Level 1	Level 2	Level 3
25	313	2649

Table 8
Number of collocation points for adaptive ANOVA method : $A/d = 0.1$, nominal dimension $N = 12$, active dimension $D_1 = N = 12$, $D_2 = 6$, $\mu = 3$, $\theta_2^1 = 5.0 \times 10^{-5}$ for Criterion 1 or $\theta_2^2 = 1.0 \times 10^{-3}$ for Criterion 2.

f_j	$f_j + f_{1,j}$	$f_j + f_{1,j} + f_{2,j}$	$f_j + f_{1,j} + f_{2,j} + f_{3,j}$
37	73	109	127

(2) We then set $\mu = 3$ and take the Gauss-Legendre quadrature points as $q_i^{1,2,3} = -\frac{3}{\sqrt{5}}, 0, \frac{3}{\sqrt{5}}, i = 1, 2, \ldots, N$ (here we use the same quadrature points for each dimensions, i.e., $q_1^{1,2,3} = q_2^{1,2,3} = \cdots = q_N^{1,2,3}$) since ξ_i are uniform random variables on $[-\sqrt{3}, \sqrt{3}]$, and the corresponding weights are $w^{1,2,3} = \frac{5}{18}, \frac{4}{9}, \frac{5}{18}$. We run the deterministic solver at the collocation points $(q_1^1, 0, \ldots, 0), (q_1^2, 0, \ldots, 0), \ldots, (0, \ldots, 0, q_N^1), (0, \ldots, 0, q_N^2), (0, \ldots, 0, q_N^3)$ to obtain the values of all first-order terms at quadrature points $q_i^{1,2,3}, i = 1, 2, \ldots, N$ from Eq. (2.11).
(3) We compute the mean and standard deviation required in the adaptivity criterion based on the value of first-order terms f_i at the quadrature points and corresponding weights to determine the active dimension D_2 for selecting the important second-order terms.
(4) We use tensor product rule to obtain new collocation points: $(q_1^1, q_2^1, 0, \ldots, 0), (q_1^1, q_2^2, 0, \ldots, 0), (q_1^1, q_2^3, 0, \ldots, 0), (q_1^2, q_2^1, 0, \ldots, 0), \ldots, (0, \ldots, 0, q_{N-1}^3, q_N^3)$ and run the deterministic solver at these the collocation points then compute the values of second-order terms at the quadrature points from Eq. (2.12).
(5) Finally, we use either Criterion 1 or Criterion 2 to decide the important second-order terms. Now the construction of the ANOVA decomposition of f with $v = 2$ is finished.

Remark 10. In the presentation of the roughness with relatively small amplitude (4.1), ξ_i are selected to be uniform random variables. We also tested Gaussian random variables and the results (mean and standard deviation) are very close with relative errors being only $\mathcal{O}(10^{-4})$. This result is consistent with the asymptotic analysis in [17]. Hence, we only use uniform random variable to demonstrate our method.

Remark 11. The reference solution is given by quasi-Monte Carlo method with 100,000 realizations. Here we use the sequence HaltonRR2 set [31]. We also used sparse grids of level 4 (17,265 collocation points) to solve the problem. The difference between these two results is so small that it does not affect the quantitative analysis shown in the next section. Therefore, we use the quasi-Monte Carlo results as the reference solution.

Fig. 12 compares the standard deviation of the extra lift and drag obtained by the sparse grid method We can see that the results by level 1 sparse grid method are the least accurate, especially for the extra drag. The results by the level 2 sparse grid method are better than those of level 1 sparse grid, especially for the estimate in the first reflection region [16], i.e., $x \in [1, 2.84]$. In the second reflection region, i.e., $x \in [2.84, 6]$ the estimates of both level 1 and level 2 sparse grid method are very close. The results of level 3 sparse grid method are better than those of the former two lower level sparse grid method. This can be observed more distinctly in the second reflection region in the plot of Fig. 12 for the standard deviation of the extra lift. The results by the adaptive ANOVA method are very close to the results by the level 3 sparse grid and, in fact, if we zoom in the plot of the extra lift we can see that the former one is slightly better than the latter. For the estimate of the standard deviation of the extra drag, it is hard to discern differences between level 2, level 3 sparse grid, and the adaptive ANOVA method. We also study the error more systematically and show the relative error of the standard deviation in Fig. 13, where "Lvl" means level, $f_j = f_0 + \sum_{j=1}^{12} f_j(x_j), f_{1,j} = \sum_{j=2}^{5} f_{1,j}(x_1, x_j), f_{2,j} = \sum_{j=3}^{6} f_{2,j}(x_2, x_j), f_{3,j} = \sum_{j=4}^{5} f_{3,j}(x_3, x_j)$, i.e., we decompose Eq. (4.6) into four parts and add them one by one to see the difference. We can see that the adaptive ANOVA method with terms $f_j + f_{1,j} + f_{2,j} + f_{3,j}$ leads to a better estimate of the standard deviation than the level 3 sparse grid. The x-axis in Fig. 13 is the number of collocation points (or sampling points) and since the deterministic solver with different collocation points costs almost the same, the computational cost of adaptive ANOVA is less than 1/20 of level 3 sparse grid method (see the

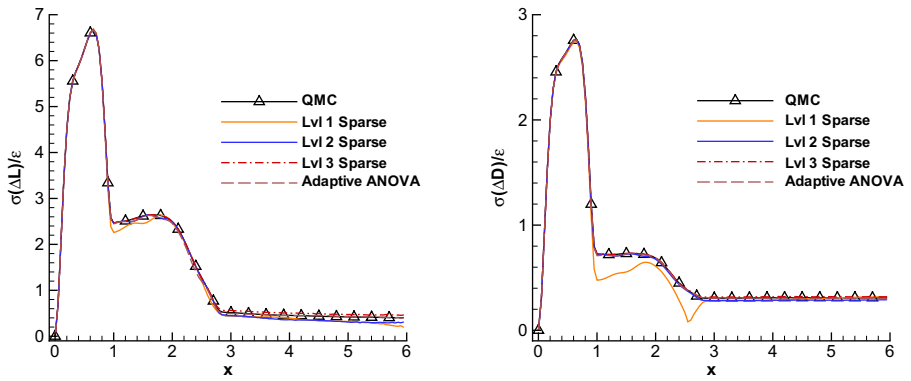

Fig. 12. Comparison of standard deviation of extra lift (left) and drag (right) for different level of sparse grid method and adaptive ANOVA method. $A = 0.1$, $D_1 = N = 12$, $D_2 = 6$, $\mu = 3$.

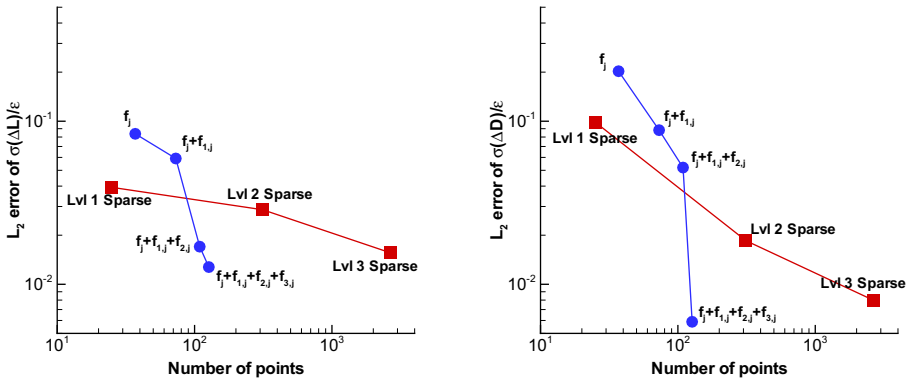

Fig. 13. Error of standard deviation of extra lift (left) and drag (right) for different level of sparse grid method and adaptive ANOVA method. $A = 0.1$, $D_1 = N = 12$, $D_2 = 6$, $\mu = 3$.

exact number of collocation points in Tables 7 and 8). Similarly, Fig. 14 compares the mean of the extra lift and drag obtained by different methods. Again, we observe that the results by the level 1 sparse grid method are worse than those of others. However, the difference between the estimate by level 2, level 3 sparse grid method, and the adaptive ANOVA method is too small to be seen on the plot so we only plot the results of adaptive ANOVA method. A systematic study of the error of the mean is presented in Fig. 15, which shows that the estimates by the adaptive ANOVA with terms $f_j + f_{1,j} + f_{2,j} + f_{3,j}$ are almost as accurate as those by level 3 sparse grid method. Moreover, Figs. 13 and 15 also show the convergence of the adaptive ANOVA method as we add the terms in Eq. (4.6) one by one. Figs. 16 and 17 show the convergence of the adaptive ANOVA

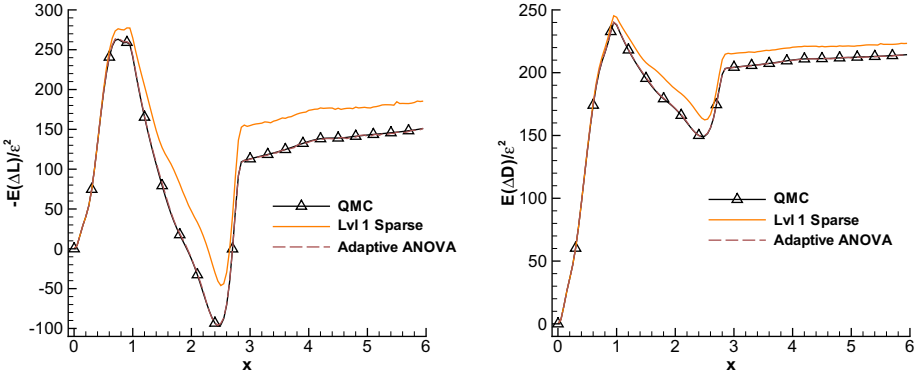

Fig. 14. Comparison of mean of extra lift (left) and drag (right) for different level of sparse grid method and adaptive ANOVA method. $A = 0.1$, $D_1 = N = 12$, $D_2 = 6$, $\mu = 3$. The curve corresponding to adaptive ANOVA coincides with the QMC curve.

method visually for the standard deviation and mean, respectively. We can see that for this case, the second-order terms play an important role in the approximation, otherwise, the results by using only f_0 and the first-order terms f_j are even worse than the level 1 sparse grid method.

Next, we compare the difference of the results by using different active dimensions listed in Table 6 (the reference solution is obtained by quasi-Monte Carlo with 50,000 realizations). Our tests show that for Criterion 1, $\theta_2^1 = 5.0 \times 10^{-5}$ is a good choice for active dimension $D_2 = 6, 7$ since it leads to small error. With this θ_2^1, when we set the active dimension to be either 6 or 7, we use the same second-order component functions, i.e., f is approximated as in (4.6). For $D_2 = 5, \theta_2^1 = 2.0 \times 10^{-5}$ is one of the optimal choices and f is approximated well by

$$f(\boldsymbol{x}) \approx f_0 + \sum_{j=1}^{12} f_j(x_j) + \sum_{j=2}^{5} f_{1,j}(x_1, x_j) + \sum_{j=3}^{5} f_{2,j}(x_2, x_j) + \sum_{j=4}^{5} f_{3,j}(x_3, x_j) + f_{4,5}(x_4, x_5). \tag{4.7}$$

Similarly, for Criterion 2, we set $\theta_2^2 = 1.0 \times 10^{-3}$ for $D_2 = 6,7$ and $\theta_2^2 = 5.0 \times 10^{-4}$ for $D_2 = 5$. With these settings, f is also approximated as in (4.6) for $D_2 = 6, 7$ and (4.7) for $D_2 = 5$. Here, we compare the results of $D_2 = 5$ and 6. The number of collocation points we use is the same, i.e., 127. The relative L_2 errors of the standard deviation and mean for the extra lift and drag are shown in Table 9. We can see that the selection of p (or $\theta_1^{1,2}$), which determines the active dimension and affects the selection of threshold $\theta_2^{1,2}$, will affect the accuracy.

We also employ a fifth-order WENO scheme [32] combined with a mapping technique for solving partial differential equations on random domains [33] to compute the numerical solution as in [17]. We use 900×300 grid points on the domain $[0,6] \times [0,0.9]$, and a steady state is achieved by time-marching. The stochastic simulations are based on the probabilistic collocation method (PCM) and both sparse grid and adaptive ANOVA are used. In Fig. 18 we observe that in the roughness region ($x \in [0,1]$) the analytical results and numerical results are almost the same. In the first reflection region ($x \in [1,2.84]$) the errors are mainly from the numerical solver as we see that the numerical results deviate from the corresponding analytical results. In the second reflection region ($x \in [2.84,6]$) the sampling error dominates as the numerical results are close to the corresponding analytical solution. Also, the difference between the results by the analytical level 1 sparse grid and the analytical adaptive ANOVA method is almost the same as the corresponding difference using the numer-

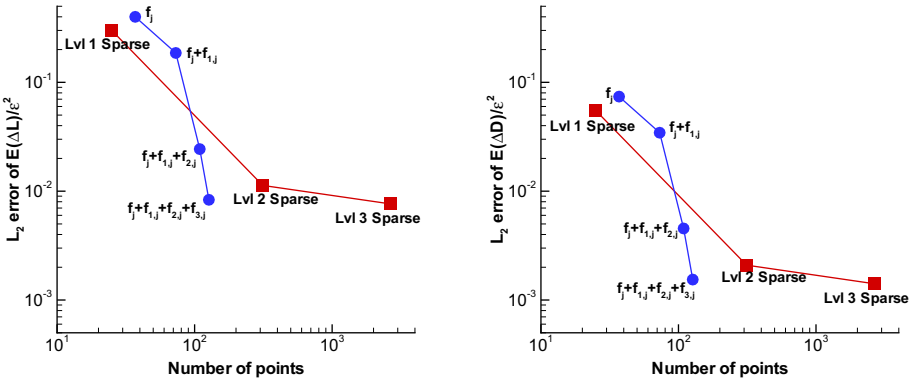

Fig. 15. Error of mean of extra lift (left) and drag (right) for different level of sparse grid method and adaptive ANOVA method. $A = 0.1$, $D_1 = N = 12$, $D_2 = 6$, $\mu = 3$.

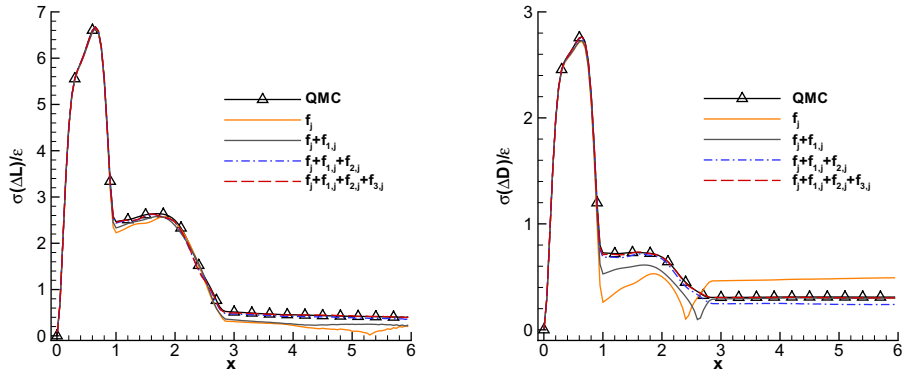

Fig. 16. Convergence of standard deviation of extra lift (left) and drag (right) for adaptive ANOVA method. $A = 0.1$, $D_1 = N = 12$, $D_2 = 6$, $\mu = 3$.

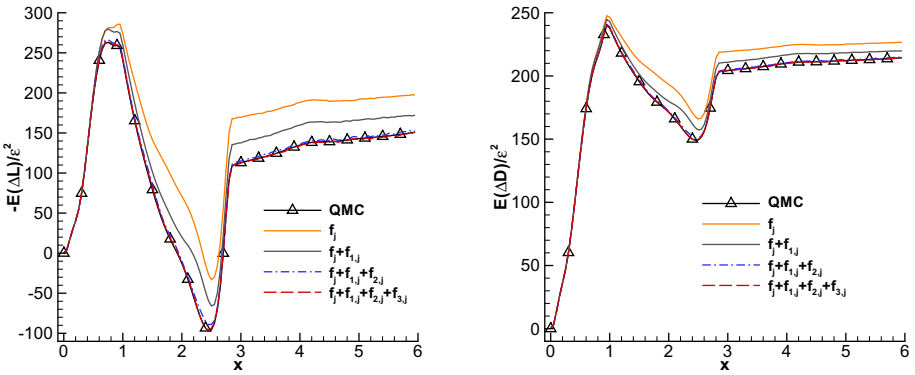

Fig. 17. Convergence of mean of extra lift (left) and drag (right) for adaptive ANOVA method. $A = 0.1$, $D_1 = N = 12$, $D_2 = 6$, $\mu = 3$.

Table 9
L_2 errors of standard deviation and mean for extra lift and drag for the adaptive ANOVA method with different active dimensions.

D_2	$\sigma(\Delta L)/\varepsilon$	$\sigma(\Delta D)/\varepsilon$	$\mathbb{E}(\Delta L)/\varepsilon^2$	$\mathbb{E}(\Delta D)/\varepsilon^2$
5	1.2967e−2	7.6705e−3	1.3198e−2	2.4486e−3
6	1.2756e−2	5.8900e−3	8.3316e−3	1.5411e−3

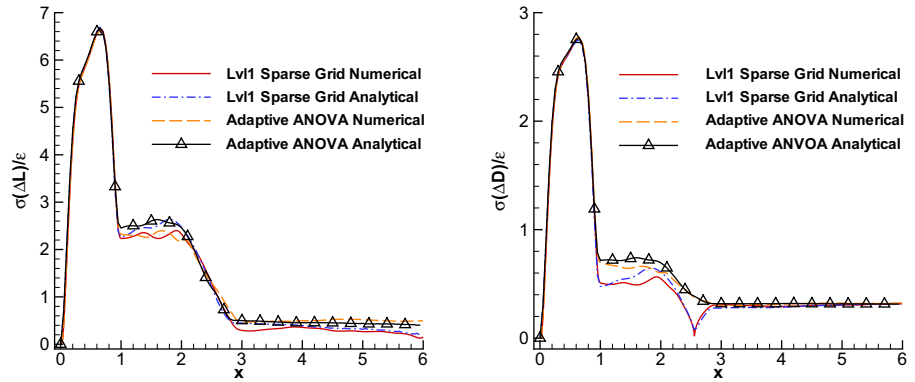

Fig. 18. Comparison of analytical solution and numerical solution of the standard deviation of extra lift (left) and drag (right) with sparse grid method and adaptive ANOVA method. $A = 0.1$, $N = 12$.

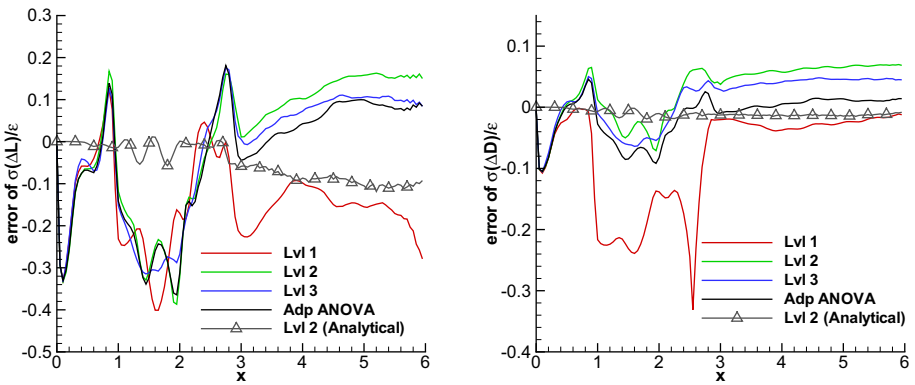

Fig. 19. Comparison of the error of standard deviation of numerical solution for extra lift (left) and drag (right) (numerical solutions minus reference solutions) with sparse grid method and adaptive ANOVA method ($f_j + f_{1,j} + f_{2,j} + f_{3,j}$). The analytical solution obtained with level 2 sparse grid is also plotted for comparison. $A = 0.1$, $N = 12$.

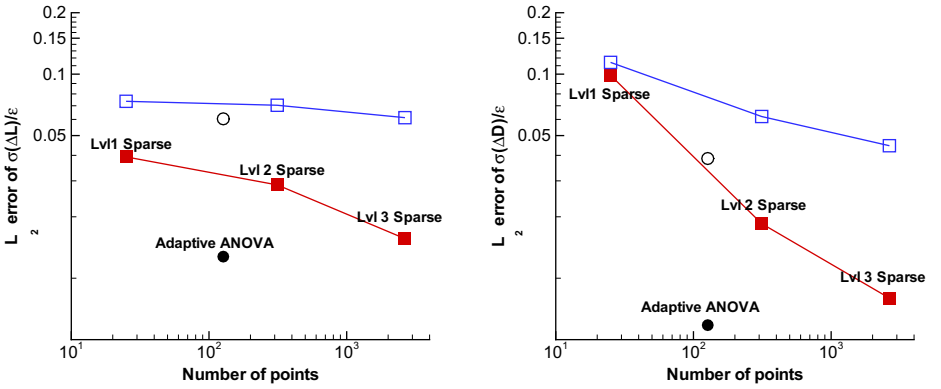

Fig. 20. Comparison of the error of standard deviation of analytical solution and numerical solution for extra lift (left) and drag (right) with sparse grid method and adaptive ANOVA method. The solid squares are errors of analytical solutions by sparse grid method; the hollow squares are errors of numerical solutions by sparse grid method; the solid circles are analytical solution by adaptive ANOVA using $f_j + f_{1,j} + f_{2,j} + f_{3,j}$; the hollow circles are numerical solution by adaptive ANOVA using $f_j + f_{1,j} + f_{2,j} + f_{3,j}$. $A/d = 0.1$, $N = 12$.

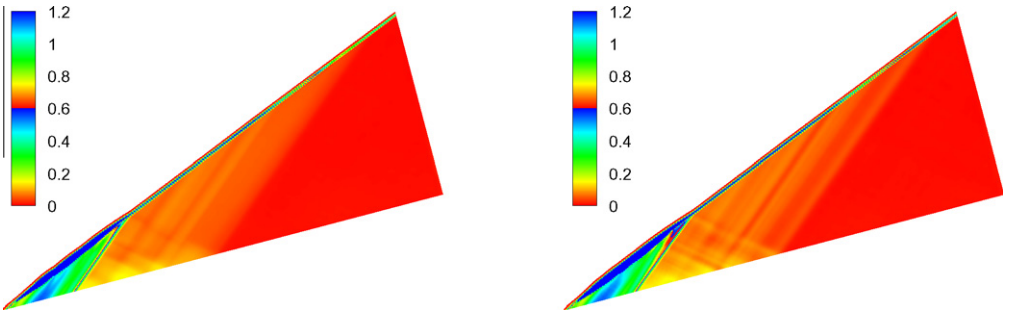

Fig. 21. Contours of the standard deviation of the normalized extra pressure by level 1 sparse grid method (left) and adaptive ANOVA method (right). $A = 0.1$, $N = 12$.

ical solver. Fig. 19 shows the errors of standard deviation of extra lift and drag (numerical solutions minus reference solutions) along the wedge obtained with different collocation points. We see that the adaptive ANOVA solutions have the smallest error compared to numerical solutions obtained from other methods. Also, we observe that near the interface $x = 1$ (where the rough surface ends) and at $x = 2.84$ (where the first reflection region ends), the numerical errors are relatively larger. Also, due to the singularity around the apex ($x = 0$), the numerical errors are relatively large close to $x = 0$. We also include the error of analytical solution obtained by the level 2 sparse grid method in Fig. 19 and compared with the numerical results we can conclude that the numerical error dominates. Fig. 20 presents the L_2 norm of the errors of the standard deviations of extra lift and drag of analytical and numerical solutions. We can observe that the gaps between the analytical solution and numerical solution reflect the numerical errors. When we increase the level of the sparse grid method, the accuracy improves only a little since the numerical errors dominate unless a finer mesh is used; however such simulations are very expensive. We also notice that the results by the adaptive ANOVA method is better than those by the level 3 sparse grid method.

A comparison of contours between level 1 sparse grid and adaptive ANOVA of the standard deviation of the extra pressure is also presented in Fig. 21. We can observe that in the roughness region, where the standard deviation is higher the shock is highly perturbed as we see in the single realization case of Fig. 2. The interface between the roughness region and the first reflection region is very distinct while the interface between the first and second reflection region is not as clear. This is similar to the single realization shown in Fig. 2. It is hard to see any difference between the two plots in Fig. 21 except that at the shock near the right end of the computational domain the standard deviation by the adaptive ANOVA method is larger than that by level 1 sparse grid method.

4.3. Small correlation length: 100 dimensions

Finally, we consider a case with correlation length 0.01 with corresponding nominal dimension $N = 100$ (about 95% in (4.5)), $\varepsilon = 1.0 \times 10^{-6}$ on physical domain [0,5]. Since the roughness height ε is very small the results by sparse grid and ANOVA are both very accurate. We only present the standard ANOVA method with $\mu = 3$, $\nu = 1$ in Fig. 22. The computational details in each step of Algorithm 1 are summarized below:

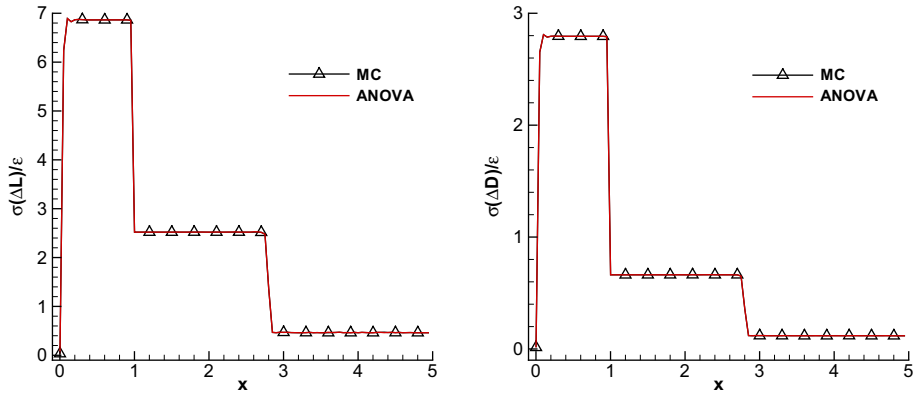

Fig. 22. Plots of standard deviation of extra lift (left) and drag (right) for ANOVA method. $A = 0.01$, $N = 100$, $\mu = 3$, $v = 1$.

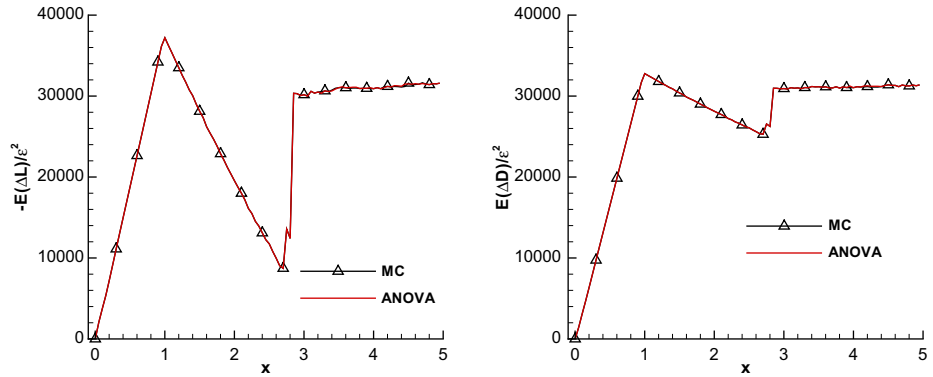

Fig. 23. Plots of mean of extra lift (left) and drag (right) for ANOVA method. $A = 0.01$, $N = 100$, $\mu = 3$, $v = 1$.

(1) We first select the anchor point $\boldsymbol{c} = 0$ and run the deterministic solver at this anchor point to obtain the constant term f_0 in the ANOVA decomposition (according to Eq. (2.8)). In this case f is the extra pressure Δp.
(2) We then set $\mu = 3$ and take Gauss-Legendre quadrature points $q_i^{1,2,3} = -\frac{3}{\sqrt{5}}, 0, \frac{3}{\sqrt{5}}, i = 1, 2, \ldots, N$ (here we use the same quadrature points for each dimensions, i.e., $q_1^{1,2,3} = q_2^{1,2,3} = \cdots = q_N^{1,2,3}$) since ξ_i are uniform random variables on $[-\sqrt{3}, \sqrt{3}]$. then the corresponding weights are $w^{1,2,3} = \frac{5}{18}, \frac{4}{9}, \frac{5}{18}$. Run the deterministic solver at the collocation points $\left(q_1^{1,2,3}, 0, \ldots, 0\right), \left(0, q_2^{1,2,3}, 0, \ldots, 0\right), \ldots, (0, \ldots, 0, q_N^{1,2,3})$ to obtain the value of all first-order terms at quadrature points $q_i^{1,2,3}, i = 1, 2, \ldots, N$ from Eq. (2.11). Since $v = 1$, at this point, the ANOVA decomposition is constructed.

Remark 12. Note that we only use first-order terms so we have fewer steps here.

We can see the results by Monte Carlo (100,000 realizations, within 95% confidence interval) and ANOVA are very close to each other. For this case, since the correlation length is small, the change of standard deviation is very sharp at $x = 1$ and $x = 2.84$, i.e., the interface of the roughness region and first reflection as well as the interface of the first and second reflection regions. Also, $x = 1$ is the peak point for the mean while $x = 2.84$ is the point where sharp change appears. Comparing Figs. 22 and 23 with Figs. 12 and 14 we can observe that a dramatic effect of correlation length on the physics of the scattering problem as the change at the interface of different regions becomes sharp (see the range of roughness region, first reflection region and second reflection region in Fig. 2). Moreover, when the correlation length is very small, e.g., 0.01, the random roughness at points between 0 and 1 can be approximately treated as independent random variables with the same variance, therefore we observe three very flat steps in the figure of the standard deviation.

5. Summary and discussion

The main result of this paper is that functional ANOVA in conjunction with a proper adaptivity strategy is a very effective dimension–reduction technique that allows simulation of stochastic flows in high dimensions. This was demonstrated for a viscous incompressible flow as well as an inviscid compressible flow, both in steady state, with stochastic perturbations of very small correlation length requiring up to 100 random dimensions. Even for a moderate number of dimensions, i.e.,

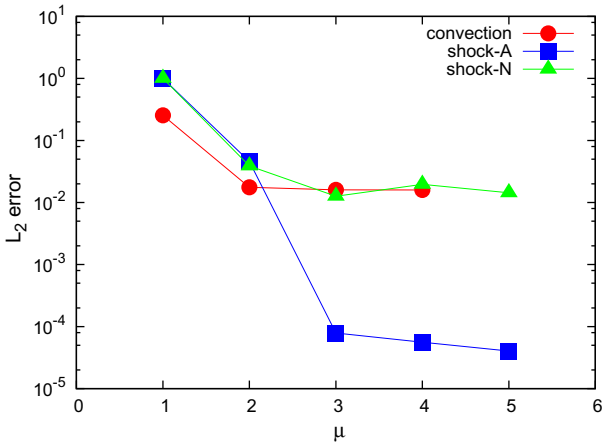

Fig. 24. Comparison of errors in standard deviations obtained by the standard ANOVA method. The absolute error of numerical result of the velocity in x-direction for the convection problem is plotted corresponding to $A = 0.1$, $N = 44$, $Ra = 5000$, $\sigma = 0.15$, $v = 1$. Both the relative errors of analytical solution (shock-A) and numerical solution (shock-N) of extra lift for the shock problem are plotted corresponding to $M_1 = 2$, $A = 1.0$, $N = 6$, $\varepsilon = 0.003$, $v = 2$.

$N \approx 10$, adaptive ANOVA is 20 times faster than sparse grids for comparable accuracy; in this case it is also three orders of magnitude faster than Monte Carlo simulations. A key concept is the *active dimension* D_i for each sub-group i of the ANOVA decomposition, which can be computed on-the-fly based on the three adaptive criteria we presented here. A more theoretical approach based on "weight-theory" (similar to quasi-Monte Carlo theory) is presented in [19], where properly defined weights measure the importance of each dimension. For the two flow examples we presented here, we demonstrated that even draconian truncations of the ANOVA decomposition, i.e., $v = 2$ or even $v = 1$ can lead to reasonably accurate estimates of the mean and the variance of the stochastic solution. Clearly, more work is required to fully appreciate the limitations of this approach, especially for time-dependent flows and turbulent flows. However, at present accurate stochastic modeling of such flows even in low dimensions has not been fully realized.

An interesting aspect of the discrete ANOVA decomposition, i.e., after approximating each ANOVA term using μ collocation points, is that for *monotonic convergence* of the expansion it is required that $\mu > v$, with the best choice $\mu = v + 1$. This was first discovered in [8] for multi-dimensional function approximation and for solving elliptic stochastic PDEs. Our work here confirms this requirement for both flow problems we studied as shown in Fig. 24. In particular, for the shock problem we present convergence results both for the analytical solution as well as the numerical solution for $v = 2$. We see that there is a very big decay of the error from $\mu = 1$ to $\mu = 3$; beyond $\mu = 3$ the convergence for the analytical solution is very slow while for the numerical solution there is no convergence. The reason for the latter behavior is the dominance of the numerical discretization error (in the physical domain); the same is true for the convection problem for which we have $v = 1$.

Finally, we note the importance of the value of the correlation length of the stochastic perturbations on the quantities of interest for each problem. For the convection problem the mean Nusselt number is not affected very much but the variance changes by almost an order of magnitude in a non-monotonic fashion as we decrease the correlation length to its smallest value, i.e., 100 times smaller than the characteristic integral length scale. In contrast, the value of correlation length affects strongly both the mean *and* the variance for the shock problem. In particular, for small ε and $A \ll 1$, the mean of the perturbed pressure scales $\propto \varepsilon^2$ and $\propto A^{-2}$ while the corresponding variance scales $\propto \varepsilon$ and $\propto A^{-1}$. However, for large ε, the mean pressure scales approximately $\propto \varepsilon$, while for $A > 1$ it is independent of A; see also [17].

Acknowledgement

GEK would like to acknowledge support by MURI/AFOSR and NSF. GEK and GL also acknowledge joint support by the Applied Mathematics program of the US DOE Office of Advanced Scientific Computing Research. Computations were performed using the computational resources of the National Energy Research Scientific Computing Center at Lawrence Berkeley National Laboratory and the William R. Wiley Environmental Molecular Sciences Laboratory (EMSL). EMSL is a DOE national scientific user facility located at PNNL. The Pacific Northwest National Laboratory is operated by Battelle for the US Department of Energy under Contract DE-AC05-76RL01830.

Appendix A. Stochastic perturbation analysis

In this section we briefly describe the first- and second-order perturbation methods to obtain analytical solutions for small roughness height; details can be found in [17]. We assume that: (1) The random wedge roughness is small, and correspondingly the perturbation of the shock slope is small. (2) The oblique shock is attached to the wedge. (3) The flow between the shock and the wedge is adiabatic.

The isentropic flow between the wedge and the shock is governed by the Euler equations along with the isentropic condition (2D case):

$$\begin{cases} u\frac{\partial p}{\partial x}+\upsilon\frac{\partial p}{\partial y}+\rho c^2\left(\frac{\partial u}{\partial x}+\frac{\partial \upsilon}{\partial y}\right)=0,\\ u\frac{\partial u}{\partial x}+\upsilon\frac{\partial u}{\partial y}+\frac{1}{\rho}\frac{\partial p}{\partial x},\\ u\frac{\partial \upsilon}{\partial x}+\upsilon\frac{\partial \upsilon}{\partial y}+\frac{1}{\rho}\frac{\partial p}{\partial y},\\ u\frac{\partial s}{\partial x}+\upsilon\frac{\partial s}{\partial y}=0, \end{cases} \tag{A.1}$$

where the first equation of Eq. (A.1) is based on the fact that $c^2=\frac{\partial p}{\partial \rho}$. On the wedge surface ($y=\varepsilon h(x;\omega)$), the slip boundary condition $\left(\frac{\upsilon_w}{u_w}=\varepsilon\frac{\partial h}{\partial x}\right)$ is employed, where υ_w and u_w are the velocity perpendicular and parallel to the wedge. According to the Rankine–Hugoniot relations, we have:

$$\begin{aligned} &\frac{P_2}{P_1}=1+\frac{2\gamma}{1+\gamma}(M_1^2\sin^2\chi-1),\quad \frac{\rho_1}{\rho_2}=\frac{u_2}{u_1}=\frac{(\gamma-1)M_1^2\sin^2\chi+2}{(\gamma+1)M_1^2\sin^2\chi},\\ &\tan(\chi-\theta)=\tan\chi\frac{(\gamma-1)M_1^2\sin^2\chi+2}{(\gamma+1)M_1^2\sin^2\chi}\equiv T(M_1,\chi). \end{aligned} \tag{A.2}$$

A.1. First-order theory

The domain we consider is between the perturbed shock and the wedge surface. We use the subscript '2' for the flow state after the shock and take the x-axis along the surface of the 'unperturbed' wedge. Let

$$\frac{u}{W_2}=1+\varepsilon w',\quad \frac{\upsilon}{W_2}=\varepsilon\upsilon,\quad \frac{p}{P_2}=1+\varepsilon p',\quad \frac{\rho}{\rho_2}=1+\varepsilon\rho',\quad \frac{s}{S_2}=1+\varepsilon s'. \tag{A.3}$$

On the wedge surface, we have $\upsilon_w'=\frac{\partial h}{\partial x}$ and using the Rankine–Hugoniot relations (Eq. (A.2)), we obtain the interface conditions after the shock:

$$\upsilon_s'=\theta'=F(M_1,x_0)\chi',\quad \frac{\sqrt{M_2^2-1}}{\gamma M_2}p_s'=G(M_1,\chi_0)\chi', \tag{A.4}$$

where

$$\begin{aligned} &F(M_1,\chi_0)\equiv\frac{\mathrm{d}\theta}{\mathrm{d}\chi}=1-\frac{1}{1+T_0^2}\frac{\partial T}{\partial\chi},\\ &G(M_1,\chi_0)\equiv\frac{\sqrt{M_2^2-1}}{\gamma M_2^2P_2}\frac{\mathrm{d}P_2}{\mathrm{d}\chi}=\frac{\sqrt{M_2^2-1}}{\gamma M_2^2}\frac{2\gamma M_1^2\sin 2\chi_0}{1-\gamma+2\gamma M_1^2\sin^2\chi_0},\\ &T=\tan(\chi-\theta),\quad T_0=\tan(\chi_0-\theta_0),\quad M_1=\frac{W_1}{c_1},\quad M_2^2=M_1^2\frac{P_1\rho_2\cos^2\chi_0}{P_2\rho_1\cos^2(\chi_0-\theta_0)}. \end{aligned} \tag{A.5}$$

To quantify the region of validity for the stochastic perturbation analysis, we use the standard deviation of the stochastic roughness as a measure. To simplify the problem with small perturbation, we have employed the following assumption:

$$\varepsilon\ll\min\left(\frac{1}{\sigma(w')},\frac{1}{\sigma(\upsilon')},\frac{1}{\sigma(\rho')},\frac{1}{\sigma(p')}\right), \tag{A.6}$$

where σ denotes the standard deviation. The region of validity with respect to the roughness amplitude ε for the stochastic perturbation analysis is discussed in Appendix C of [17]. Substituting Eq. (A.6) into the steady Euler Eq. (A.1) we obtain the linearized small perturbation equations:

$$\begin{cases} \frac{\partial \upsilon'}{\partial y}+\frac{M_2^2-1}{\gamma M_2^2}\frac{\partial p'}{\partial x}=0,\\ \frac{\partial}{\partial x}\left(w'+\frac{1}{\gamma M_2^2}p'\right)=0,\\ \frac{\partial \upsilon'}{\partial x}+\frac{1}{\gamma M_2^2}\frac{\partial p'}{\partial y}=0,\\ \frac{\partial}{\partial x}(p'-\gamma\rho')=0. \end{cases} \tag{A.7}$$

The results for the first-order method are:

$$\chi'(x;\omega)=q\sum_{n=0}^{\infty}(-r)^n\frac{\partial h}{\partial x}(x;\omega)\Big|_{x=\alpha\beta^n x}, \tag{A.8}$$

where

$$q=\frac{2}{F+G},\quad r=\frac{F-G}{F+G},\quad \alpha=1-\frac{T_0}{m},\quad \beta=\frac{m-T_0}{m+T_0},\quad m=\frac{1}{\sqrt{M_2^2-1}}.$$

The perturbed pressure p'_w on the rough wedge surface is:

$$p'_w(x;\omega)=\frac{\gamma M_2^2}{\sqrt{M_2^2-1}}\left(\frac{\partial h(x;\omega)}{\partial x}+2\sum_{n=1}^{\infty}(-r)^n\frac{\partial h}{\partial x}\Big|_{x=\beta^n x}\right). \tag{A.9}$$

The perturbed shock path z' is computed by:

$$z'(x;\omega)=(1+T_0^2)\int_0^x \chi'(x_1;\omega)\,\mathrm{d}x_1. \tag{A.10}$$

Furthermore, the perturbed p', v', ρ' and w' at any location (x,y) after the shock can also be obtained (see [17]).

A.2. Second-order theory

Using an iterative procedure we start with $z'(x;\omega)$ (Eq. (A.10)) and $p'_w(x;\omega)$ (Eq. (A.9)) and upon convergence we obtain the corrected perturbed shock path $\widetilde{z'}(x;\omega)$ and corresponding corrected pressure $\widetilde{p'_w}(x;\omega)$. To this end, we have to re-define β in Eq. (A.9), i.e., $\beta = x_m/x$, where x_m,x are the distances from the apex of a reflection pair of points on the wedge surface ($x_m < x$). Let

$$\frac{u}{W_2}=1+\Delta w,\quad \frac{v}{W_2}=\Delta v,\quad \frac{p}{P_2}=1+\Delta p,\quad \frac{\rho}{\rho_2}=1+\Delta\rho,\quad \frac{s}{S_2}=1+\Delta s,$$

where $\Delta w=\varepsilon\widetilde{w'}+\varepsilon^2 w''$, etc., are the total first- and second-order corrections. The second-order small perturbation equations are:

$$\begin{cases}\frac{\partial v''}{\partial y}+\frac{M_2^2-1}{\gamma M_2^2}\frac{\partial p''}{\partial x}=R_1(x,y),\\ \frac{\partial}{\partial x}\left(w''+\frac{1}{\gamma M_2^2}p''\right)=R_2(x,y),\\ \frac{\partial v''}{\partial x}+\frac{1}{\gamma M_2^2}\frac{\partial p''}{\partial y}=R_3(x,y),\\ \frac{\partial}{\partial x}(p''-\gamma\rho'')=R_2(x,y),\end{cases} \tag{A.11}$$

where

$$\begin{aligned}R_1(x,y)&=-\frac{1}{\gamma M_2^2}\left(-M_2^2\widetilde{p'}+\widetilde{\rho'}+\left(M_2^2+1\right)\widetilde{w'}\right)\frac{\partial\widetilde{w'}}{\partial x}+v'\left(\frac{\partial\widetilde{w'}}{\partial y}-\frac{1}{\gamma}\frac{\partial\widetilde{p'}}{\partial y}\right),\\ R_2(x,y)&=\frac{(\widetilde{w'}+\widetilde{\rho'})}{\gamma M_2^2}\frac{\partial\widetilde{p'}}{\partial x}-v'\frac{\partial\widetilde{w'}}{\partial y},\\ R_3(x,y)&=\frac{1}{\gamma M_2^2}\left(\left(\widetilde{w'}+\widetilde{\rho'}\right)\frac{\partial\widetilde{p'}}{\partial y}+\left(M_2^2-1\right)v'\frac{\partial\widetilde{p'}}{\partial x}\right),\\ R_4(x,y)&=\frac{1}{2}\frac{\partial}{\partial x}(\widetilde{p'}^2-\gamma\widetilde{\rho'}^2)-v'\frac{\partial}{\partial y}(\widetilde{p'}-\gamma\widetilde{\rho'}).\end{aligned}$$

We note that the ~ denotes a converged first-order state that is corrected due to the shock path update. According to the Rankine–Hugoniot relations, we obtain p''_s and v'_s on the shock path based on the first-order corrected shock path:

$$v''_s=F(M_1,\chi_0)\chi''+F_2(M_1,\chi_0)\widetilde{\chi'}^2,\quad \frac{\sqrt{M_2^2-1}}{\gamma M_2^2}p''_s=G(M_1,\chi_0)\chi''+G_2(M_1,\chi_0)\widetilde{\chi'}^2,$$

where

$$\begin{aligned}G_2(M_1,\chi_0)&=\frac{2M_1^2\sqrt{M_2^2-1}\cos^2\chi_0}{M_2^2\left(1-\gamma+2\gamma M_1^2\sin^2\chi_0\right)},\\ F_2(M_1,\chi_0)&=-\frac{1}{2\left(1+T_0^2\right)}\frac{\partial^2 T}{\partial\chi^2}+T_0(1-F(M_1,\chi_0))^2+F(M_1,\chi_0)Q(M_1,\chi_0),\\ Q(M_1,\chi_0)&=\frac{2\cos(\chi_0-\theta_0)\left(\sin\theta_0-M_1^2\sin^2\chi_0\sin(2\chi_0-\theta_0)\right)}{(\gamma+1)M_1^2\cos\chi_0\sin^2\chi_0}.\end{aligned}$$

It can be shown [17] that

$$\chi''(x;\omega)=\sum_{n=0}^{\infty}(-r)^n\Big[-r_2\widetilde{\chi'}^2(\beta^n x;\omega)-r_3\widetilde{\chi'}^2(\beta^{n+1}x;\omega)+2r_4\upsilon_w''(\alpha\beta^n x;\omega)\\ +r_4\left(\int_{\alpha\beta^n x}^{\beta^n x}R_+(x_1,mx_1)\,dx_1-\int_{\beta^{n+1}x}^{\alpha\beta^n x}R_-(x_1,-mx_1)\,dx_1\right)\Big], \tag{A.12}$$

where

$$\upsilon_w''(x;\omega)=\widetilde{w_w'}(x;\omega)\frac{\partial h(x;\omega)}{\partial x},\quad r_2=\frac{F_2+G_2}{F+G},\quad r_3=\frac{F_2-G_2}{F+G},\quad r_4=\frac{1}{F+G},$$
$$R_\pm(x_1,y_1)=R_3(x_1,y_1)\pm\frac{1}{\sqrt{M_2^2-1}}R_1(x_1,y_1).$$

The second-order perturbation equations for pressure is

$$p_w''(x;\omega)=\frac{\gamma M_2^2}{\sqrt{M^2-1}}\sum_{n=0}^{\infty}(-r)^n\left[2\frac{FG_2-F_2G}{F+G}\widetilde{\chi'}^2\left(\frac{\beta^{n+1}}{\alpha}x;\omega\right)\right.\\ \left.+\upsilon_w''(\beta^n;\omega)-r\upsilon_w'(\beta^{n+1}x;\omega)-r\int_{\beta^{n+1}x}^{\frac{\beta^{n+1}}{\alpha}x}R_+(x_1,mx_1)\,dx_1-\int_{\frac{\beta^{n+1}}{\alpha}x}^{\beta^n x}R_-(x_1,-mx_1)\,dx_1\right]. \tag{A.13}$$

while the shock path is

$$z(x;\omega)=\varepsilon\widetilde{z'}+\varepsilon^2z''=\varepsilon(1+T_0^2)\int_0^x\widetilde{\chi'}+\varepsilon(\chi''+T_0\widetilde{\chi'}^2\,dx_1), \tag{A.14}$$

where $\widetilde{z'}$ and z'' are defined implicitly here. Hence the perturbed pressure on the wedge surface is given by

$$\Delta p_w(x;\omega)=\varepsilon\widetilde{p'}+\varepsilon^2p_w''. \tag{A.15}$$

We note that $\Delta p_w, \widetilde{p'}_w, p_w''$ are normalized by P_2, which is the pressure of the base flow after the shock. Based on these expressions for pressure, we can determine the perturbed lift and drag force on the wedge (non-dimensionalized by P_2d):

$$\Delta L(x;\omega)=\varepsilon\left[h\sin\theta_0-\cos\theta_0\int_0^x\widetilde{p'}_w\,dx_1+\varepsilon\int_0^x\left(\widetilde{p'}_w\frac{\partial h}{\partial x_1}\sin\theta_0-p_w''\cos\theta_0\right)dx_1\right],\\ \Delta D(x;\omega)=\varepsilon\left[h\cos\theta_0+\sin\theta_0\int_0^x\widetilde{p'}_w\,dx_1+\varepsilon\int_0^x\left(\widetilde{p'}_w\frac{\partial h}{\partial x_1}\cos\theta_0+p_w\sin\theta_0\right)dx_1\right]. \tag{A.16}$$

A.3. A simple example

Here we give a very simple example to demonstrate the procedure of estimating the mean and variance of a function by considering a 3-dimensional Sobol function :

$$f(\boldsymbol{x})=\prod_{k=1}^{3}f^{(k)}(x_k),\quad f^{(k)}(x_k)=\frac{|4x_k-2|+k^2}{1+k^2}, \tag{A.17}$$

where x_k are i.i.d. random variables and $x_k\sim U[0,1]$. It is easy to obtain that $\mathbb{E}(f)=1,\sigma^2(f)=0.1014$. For the anchored-ANOVA decomposition, we choose an anchor point $\boldsymbol{c}=(c_1,c_2,c_3)$ such that $f^{(k)}(c_k)=(0.1\lambda_k^2+\tau_k^2)/\tau_k$ and as in Example 1, τ_k and λ_k^2 are the mean and variance of $f^{(k)}$. We set $\mu=4$, i.e., for each x_k we use four sampling points q_i, $i=1,2,3,4$, which are selected as follows: q_1, q_2 are Gauss quadrature points on $[0,0.5]$, and q_3, q_4 are Gauss quadrature points on $[0.5,1]$. Notice that, this is only for demonstration purposes; for practical problems, one can either use quadrature points on the entire domain or select quadrature points based on the property of the problem itself.

We first compute f_0:

$$f_0=f(\boldsymbol{c})=\prod_{k=1}^{3}f^{(k)}(c_k)=\prod_{k=1}^{3}\frac{0.1\lambda_k^2+\tau_k^2}{\tau_k}=1.010.$$

Then, we compute $f_j(q_i)$, $j=1,2,3$, $i=1,2,3,4$, e.g.,

$$f_1(q_2)=f(q_2,c_2,c_3)-f_0.$$

Table A.10
Mean and variance of the first-order terms in anchored-ANOVA decomposition of $f(x)$ in (A.17).

	f_1	f_2	f_3
$\mathbb{E}$	−8.3472e−3	−1.3449e−3	−3.3656e−4
σ^2	8.3611e−2	1.3566e−2	3.3982e−3

Hence the mean and variance of f_j can be estimated:

$$\mathbb{E}(f_j) \approx \sum_{i=1}^{4} f_1(q_i)w_i, \quad \sigma^2(f_j) \approx \sum_{i=1}^{4} \left(f_j(q_i)\right)^2 w_i - \left(\sum_{i=1}^{4} f_j(q_i)w_i\right)^2.$$

The results are shown in Table A.10 As in the paper we set $D_1 = N = 3$, then we can apply the criteria to find D_2.

Criterion 1:

$$\frac{\sum_{i=1}^{1}\sigma^2(f_i)}{\sum_{i=1}^{3}\sigma^2(f_i)} = 0.8313, \quad \frac{\sum_{i=1}^{2}\sigma^2(f_i)}{\sum_{i=1}^{3}\sigma^2(f_i)} = 0.9662, \quad \frac{\sum_{i=1}^{3}\sigma^2(f_i)}{\sum_{i=1}^{3}\sigma^2(f_i)} = 1,$$

or equivalently consider

$$\frac{\sigma^2(f_1)}{\sum_{i=1}^{3}\sigma^2(f_i)} = 0.8313, \quad \frac{\sigma^2(f_2)}{\sum_{i=1}^{3}\sigma^2(f_i)} = 0.1349, \quad \frac{\sigma^2(f_3)}{\sum_{i=1}^{3}\sigma^2(f_i)} = 0.0338.$$

So if we set $p = 0.85$ (or $\theta_1^1 = 0.2$ for instance) we have $D_2 = 1$ while if we set $p = 0.90$ (or $\theta_1^1 = 0.1$) we have $D_2 = 2$. From this criterion we observe that x_1 is the most important while x_3 is the least important.

Criterion 2:

$$\frac{|\mathbb{E}(f_1)|}{|f_0|} = 8.264e-3, \quad \frac{|\mathbb{E}(f_2)|}{|f_0|} = 1.332e-3, \quad \frac{|\mathbb{E}(f_3)|}{|f_0|} = 3.332e-4.$$

So if we set $\theta_1^2 = 1e-3$ we have $D_2 = 2$ while if we set $\theta_1^2 = 1e-4$ we have $D_2 = 3$. From this criterion we again observe that x_1 is the most important while x_3 is the least important.

Criterion 3:

$$\gamma_1 = 13/12, \quad \gamma_2 = 76/75, \quad \gamma_3 = 301/300.$$

Here we see that Criterion 3 gives the same prediction as Criterion 1 or Criterion 2.

According to Criterion 1 or Criterion 2, $D_2 = 1$ or $D_2 = 2$ for different thresholds. When $D_2 = 1$, no second-order terms will be included. Therefore, the approximation for f is:

$$f(\boldsymbol{x}) \approx f_0 + f_1(x_1) + f_2(x_2) + f_3(x_3).$$

Now we can approximate $\mathbb{E}(f)$ by the sum of the mean of all the component functions and so we approximate $\sigma^2(f)$ similarly. The error of $\mathbb{E}(f)$ is 1.43e−5 and the error of $\sigma^2(f)$ is 8.62e−4.

In order to include the second-order terms, we proceed as follows.

Criterion 1: since $D_2 = 2$ we only need $f_{1,2}$ and if $D_2 = 3$ we compute

$$\frac{\sigma^2(f_{1,2})}{\sum_{i=1}^{3}\sigma^2(f_i)} = 1.107e-2, \quad \frac{\sigma^2(f_{1,3})}{\sum_{i=1}^{3}\sigma^2(f_i)} = 2.772e-3, \quad \frac{\sigma^2(f_{2,3})}{\sum_{i=1}^{3}\sigma^2(f_i)} = 4.494e-4.$$

We observe here that the interaction of x_1 and x_2 is the most important. If we set $\theta_2^1 = 0.1$ we obtain the approximation:

$$f(\boldsymbol{x}) \approx f_0 + f_1(x_1) + f_2(x_2) + f_3(x_3) + f_{1,2}(x_1, x_2).$$

Criterion 2: similar to the case of Criterion 1, since $D_2 = 2$ we only need $f_{1,2}$ and if $D_2 = 3$ we compute

$$\frac{\mathbb{E}(f_{1,2})}{\sum_{i=0}^{3}|\mathbb{E}(f_i)|} = 1.089e-5, \quad \frac{\mathbb{E}(f_{1,3})}{\sum_{i=0}^{3}|\mathbb{E}(f_i)|} = 2.727e-6, \quad \frac{\mathbb{E}(f_{2,3})}{\sum_{i=0}^{3}|\mathbb{E}(f_i)|} = 4.393e-7.$$

We observe that again the interaction of x_1, x_2 is the most important. If we set $\theta_2^2 = 1e-5$ for Criterion 2, we obtain the same approximation as in Criterion 1:

$$f(\boldsymbol{x}) \approx f_0 + f_1(x_1) + f_2(x_2) + f_3(x_3) + f_{1,2}(x_1, x_2).$$

For this approximation, the error of $\mathbb{E}(f)$ is 3.26e−6 and the error of $\sigma^2(f)$ is 2.51e−4.

Criterion 3: we set $D_2 = 3$ and compute

$$\frac{\gamma_1\gamma_2}{1+\sum_{i=1}^{3}\gamma_i+\sum_{j\neq k}\gamma_j\gamma_k}=1.009e-3,\quad \frac{\gamma_1\gamma_3}{1+\sum_{i=1}^{3}\gamma_i+\sum_{j\neq k}\gamma_j\gamma_k}=2.522e-4,\quad \frac{\gamma_2\gamma_3}{1+\sum_{i=1}^{3}\gamma_i+\sum_{j\neq k}\gamma_j\gamma_k}=4.035e-5.$$

Again, we observe the same importance order as in *criteria 1* and 2.

References

[1] X. Wang, I. Sloan, Why are high-dimensional finance problems often of low effective dimension?, SIAM J Sci. Comp. 27 (1) (2005) 159–183.
[2] I. Sloan, When are Quasi-Monte Carlo algorithms efficient for high-dimensional integrals?, J Complex. 14 (1998) 1–33.
[3] M. Griebel, Sparse grids and related approximation schemes for higher-dimensional problems, in: Proceedings of the Conference on Foundations of Computational Mathematics, Santander, Spain, 2005.
[4] M. Bieri, C. Schwab, Sparse high order FEM for elliptic SPDES, Comput. Methods Appl. Mech. Eng. 198 (2009) 1149–1170.
[5] R. Fisher, Statistical Methods for Research Workers, Oliver and Boyd, 1925.
[6] W. Hoeffding, A class of statistics with asymptotically normal distributions, Ann. Math. Statist. 19 (1948) 293–325.
[7] C. Winter, A. Guadagnini, D. Nychka, D. Tartakovsky, Multivariate sensitivity analysis of saturated flow through simulated highly heterogeneous groundwater aquifers, J. Comput. Phys. 217 (2009) 166–175.
[8] J.Y. Foo, G.E. Karniadakis, Multi-element probabilistic collocation in high dimensions, J. Comput. Phys. 229 (2009) 1536–1557.
[9] X. Ma, N. Zabaras, An adaptive hierarchical sparse grid collocation method for the solution of stochastic differential equations, J. Comput. Phys. 228 (2009) 3084–3113.
[10] L.A. Segel, Distant side-walls cause slow amplitude modulation of cellular convection, J. Fluid Mech. 38 (1) (1969) 203–224.
[11] P. Hall, I.C. Walton, The smooth transition to a convective regime in a two-dimensional box, Proc. Roy. Soc. Lond. A 358 (1978) 199–221.
[12] Y.A. Gelfgat, Different modes of Rayleigh–Bénard instability in two and three dimensional rectangular enclosures, J. Comput. Phys. 156 (1999) 300–324.
[13] D. Venturi, X. Wan, G.E. Karniadakis, Stochastic bifurcation analysis of Raylaigh–Bénard convection, J. Fluid Mech. 650 (2010) 391–413.
[14] M. Lighthill, The flow behind a stationary shock, Philos. Mag. 40 (1949) 214–220.
[15] B.-T. Chu, On weak interaction of strong shock and mach waves generated downstream of the shock, J. Aeronaut. Sci. 19 (7) (1952) 433–446.
[16] G. Lin, C.-H. Su, G.E. Karniadakis, Random roughness enhances lift in supersonic flow, Phys. Rev. Lett. 99 (2007) 104501.
[17] G. Lin, C.-H. Su, G.E. Karniadakis, Stochastic modeling of random roughness in shock scattering problems: theory and simulations, Comput. Methods Appl. Mech. Eng. 197 (2008) 3420–3434.
[18] I. Sobol', Global sensitivity indices for nonlinear mathematical models and their monte carlo estimates, Math. Comput. Simul. 55 (2001) 271–280.
[19] Z. Zhang, M. Choi, G.E. Karniadakis, Anchor points matter in anova decomposition, in: Spectral and High Order Methods for Partial Differential Equations Lecture Notes in Computational Science and Engineering, vol. 76, Springer, 2011, pp. 347–355.
[20] Z. Zhang, M. Choi, G.E. Karniadakis, Error estimates for the anova method with polynomial choas interpolation: tensor product functions, SIAM J. Sci. Comput., submitted for publication.
[21] X. Ma, N. Zabaras, An adaptive high dimensional stochastic model representation technique for the solution of stochastic partial differential equations, J. Comput. Phys. 299 (2010) 3884–3915.
[22] H. Xu, S. Rahman, A generalized dimension–reduction method for multidimensional integration in stochastic mechanics, Int. J. Numer. Methods Eng. 61 (12) (2004) 1992–2019.
[23] R. Caflisch, W. Morokoff, A. Owen, Valuation of mortgage-backed securities using Brownian bridges to reduce the effective dimension, J. Comput. Finance 1 (1997) 27–46.
[24] O. Le Maître, M.T. Reagan, B. Debusschere, H.N. Najm, R.G. Ghanem, O.M. Knio, Natural convection in a closed cavity under stochastic non-Boussinesq conditions, SIAM J. Sci. Comput. 26 (2) (2005) 375–394.
[25] B. Ganapathysubramanian, N. Zabaras, Sparse grid collocation schemes for stochastic natural convection problems, J. Comput. Phys. 225 (1) (2007) 652–685.
[26] D. Venturi, X. Wan, G.E. Karniadakis, Stochastic low-dimensional modelling of a random laminar wake past a circular cylinder, J. Fluid Mech. 606 (2008) 339–367.
[27] R.M. Cotta, Integral Transforms in Computational Heat and Fluid Flow, CRC Press, Boca Raton, FL, 1993.
[28] M.A. Leal, H.A. Machado, R.M. Cotta, Integral transform solutions of transient natural convection in enclosures with variable fluid properties, Int. J. Heat Mass Transfer 43 (2000) 3977–3990.
[29] O. Chapelle, J. Weston, B. Schölkopf, Cluster Kernels for Semi-Supervised Learning, vol. 15, MIT Press, 2003. pp. 585–592.
[30] A.J. Smola, R. Kondor, Kernels and regularization on graphs, in: Learning theory and Kernel Machines: 16th annual Conference on Learning Theory, Springer, 2003, pp. 144–172.
[31] L. Kocis, W.J. Whiten, Computational investigations of low-discrepancy sequences, ACM Trans. Math. Softw. 23 (1997) 266–294.
[32] G.-S. Jiang, C.-W. Shu, Efficient implementation of weighted eno schemes, J. Comput. Phys. 126 (1996) 202–228.
[33] D. Xiu, D. Tartakovsky, Numerical methods for differential equations in random domains, SIAM J. Sci. Comput. 28 (3) (2006) 1167–1185.